

1

2

3

4

5

6

7

8

9

10 ^a University of Utah, Department of Chemical Engineering, 50 South Central Campus Dr., 3290
11 MEB, Salt Lake City, UT 84112-9203, USA

12

13 Corresponding Author: Kody M. Powell, Email: kody.powell@utah.edu, Tel: +1-801-581-3957

Abstract

Solar power is considered among the leading renewable energy technologies. Abundant supply, flexibility of installation, and decreasing cost makes it an interesting renewable energy resource. However, there are challenges associated with the reliability of solar power due to its intermittent nature. This work demonstrates the synergies that exist in integrated hybrid systems, where a dispatchable fuel is used in conjunction with concentrated solar power. In this simulation-based study, a parabolic trough solar concentrator is used to collect solar energy. The heat collected from the solar field is used to generate steam in a Rankine cycle. The system also utilizes natural gas combustion in the steam generator to provide supplemental steam when the solar intensity is reduced due to cloud cover or at night. Natural gas is also used for superheating the steam, which allows the system to produce higher temperatures and achieve increased thermodynamic cycle efficiencies. This flexible design produces 100 MW at nominal conditions, while it is capable of producing a maximum of 140 MW when sufficient solar energy is available. The novel contributions of this work include a complete, systems-level, dynamic model of a hybrid solar plant. The model is complete with a control system that smoothly transitions the plant from pure natural gas mode at night to solar hybrid mode during the day. It evaluates innovative design features such as flexible fuel operation, steam superheating to boost efficiency, and preheating by solar or waste heat. Furthermore, this work demonstrates that by hybridizing a solar system with a dispatchable energy source, both the reliability and efficiency of the solar power production are increased. The annual solar-to-electric efficiency increases from 15.2% to 26.13% with hybridization, which indicates that utilization of the solar energy is effectively increased.

Keywords: concentrated solar power, natural gas plant, hybrid system, dynamic simulation and control

45 **Nomenclature**

| | | |
|----|---------------|---|
| 46 | T | temperature |
| 47 | t | time |
| 48 | x | length |
| 49 | \dot{m} | mass flow rate |
| 50 | C | heat capacity |
| 51 | P | pressure |
| 52 | T | temperature |
| 53 | \hat{P} | perimeter |
| 54 | A | area |
| 55 | V | volume |
| 56 | ρ | density |
| 57 | h | heat transfer coefficient |
| 58 | HTF | heat transfer fluid |
| 59 | fb | firebox |
| 60 | SFB | secondary firebox |
| 61 | Q | heat radiation |
| 62 | Conv | convective |
| 63 | comb | combustion |
| 64 | Eff | efficiency |
| 65 | Gen | generator |
| 66 | R_{te} | resistance between tube and envelope |
| 67 | q | solar power |
| 68 | r | radius |
| 69 | σ | Stefan Boltzman constant |
| 70 | ε | emissivity |
| 71 | HP | high pressure |
| 72 | LP | low pressure |
| 73 | IP | intermediate pressure |
| 74 | STE | solar-to-electric efficiency |
| 75 | BFW | boiler feed water |
| 76 | abs | absorber |
| 77 | g | glass |
| 78 | sh | superheated |
| 79 | rh | reheated |
| 80 | $R_{abs,g}$ | thermal resistance between the absorber tube and the glass envelope |
| 81 | η | efficiency |

83

84

85

86

1. Introduction

87

88

89

90

91

92

93

94

95

96

97

98

99

The world is in need of reliable and cost effective renewable energy sources for a sustainable and cleaner future. While solar and wind show great promise and are decreasing in cost, they are variable in nature and cannot yet be entirely relied upon to meet the energy demand of consumers on a large scale. This requires dispatchable energy sources to serve as a backup. Natural gas is currently a low cost, abundant, and relatively clean fuel source and holds much promise as a fuel that can aid in the transition to a renewable energy economy over the next several decades. While fossil fuels, renewables, and other energy sources are generally combined at the grid level to collectively meet electricity demand, hybridizing energy sources at the plant level is not commonly implemented. Hybridization, however, can allow a plant to exploit the benefits of multiple energy sources. Solar thermal power, which harnesses the energy of the Sun to create heat, utilizes conventional power generation equipment. Because of this fact, solar thermal can be easily integrated with other fuel sources [1], [2]. These sources include gas, coal, biofuel, wind, photovoltaics, nuclear, etc. A summary of recent literature studying various hybridization schemes of solar thermal power with these other fuel sources can be found in [1].

100

101

102

103

104

105

106

107

108

109

110

111

Hybridization of solar thermal power with a dispatchable fuel, such as natural gas, can also benefit conventional thermal plants by offsetting the emissions and fuel costs, achieved from supplementing the thermal plant with sustainable solar energy [3], [4]. Such plants can be designed with expandable solar capacity by increasing the size of the solar field and adding thermal energy storage [5], [6]. This would allow the plant to gradually transition to a predominantly solar plant, while utilizing low cost and reliable natural gas in the interim. Additionally, hybridizing solar plants with fossil or biofuel can reduce the economic and technical barriers associated with a pure solar plant [7]. Although solar energy has experienced a substantial reduction in cost in recent years, it is still substantially more expensive than the fossil fuel-based power generation systems for baseload power generation. Hence, it is economically beneficial to hybridize the solar plants with fossil fuel-fired plants [8], [9]. Alternatively, in order to achieve completely renewable energy, bio-derived fuels can also be combined with solar thermal power in a hybrid configuration.

112

113

114

115

116

117

118

A critically important benefit to hybridizing the solar plants is the substantially increased reliability of the plant due to the addition of a dispatchable fuel. This benefit becomes obvious for a solar plant technology such as concentrated solar power (CSP). CSP is a mature technology that has synergy with conventional power generation equipment [10]. CSP technologies also have many benefits with respect to large-scale electricity production, unlike the photovoltaic technology, while it also enables low cost thermal energy storage (TES) [11], [12]. The reliability issue associated with the intermittent nature of the CSP technology can be resolved by integrating it with a fossil or biofuel-fired power generation

119 unit. This hybrid plant can rely mostly on the solar power during the day while fossil fuel can ensure a
120 continuous supply of power during the night and cloudy periods, assuming that the system is designed
121 correctly. Hybridization allows the plant to continuously produce power, as opposed to a stand-alone CSP
122 plant that produces power only during daylight hours (in absence of a substantial TES system) [13], [14].
123 A strongly synergistic plant will also allow the solar and fuel components of the system to effectively
124 share pieces of equipment, such as a boiler and steam turbine. Sharing equipment also results in a
125 reduction of the overall capital cost for the system.

126 A key field of research is the design of hybrid plants at the systems level. For instance,
127 hybridizing the parabolic trough with a combustible fuel can provide external steam superheating. This
128 allows the plant to rely on this fuel to achieve the higher temperatures required for a more efficient power
129 cycle, while allowing the solar collector to operate closer to its optimal temperature. The efficiency
130 gained by hybridization reduces the required solar area and the capital cost of the plant [15]. The
131 flexibility of hybridizing a solar plant with a dispatchable fuel also leads to opportunities for optimizing
132 the operation. To achieve this, the solar portion of the plant can be operated at or near its optimal point,
133 depending on the ambient conditions [16]. This permits harvesting the maximum amount of solar energy
134 while also reducing the need for the fuel. Additionally, studies have shown that during periods of low
135 solar availability, it is more efficient to run the solar field at low outlet temperatures, which reduces
136 radiative heat losses. In such circumstances, a combustible fuel is utilized to supply a portion of the
137 electricity load and ensure continuous power production [17], [18].

138 Using solar power and natural gas synergistically in a Rankine cycle is a promising concept due
139 to the inexhaustible supply of solar energy [7], [19] and the existence of well-developed steam-based
140 power generation technologies. A popular solar and natural gas hybrid configuration is the Integrated
141 Solar and Combined Cycle (ISCC) concept. This concept uses the efficient combined cycle technology of
142 a natural gas combustion turbine with waste heat recovery to produce steam for additional power
143 generation. This technology can seamlessly incorporate solar energy by using a solar field to produce
144 additional steam to augment to bottoming cycle of an ISCC configuration [20], [21]. In fact, there are a
145 wide variety of hybrid configurations that have been explored in literature, with a thorough review
146 provided in [1]. However, there is still a great research need for the development of hybrid energy
147 systems to maximize the overall benefit.

148 The study presented in this work has multiple objectives. This study presents a novel design of a
149 parabolic trough-based solar thermal and natural gas hybrid power plant. A key design objective is to
150 create a system that improves the solar-to-electric efficiency (STE), defined as the ratio of solar power to
151 the available solar energy, by effectively combining solar energy with fuel-based energy. The design

152 presented in this work has several innovative features. It has a dual source boiler that uses a gas-fired
153 primary firebox for steam generation and superheating when the plant is in natural gas mode. In solar
154 mode, the primary firebox is unnecessary as solar provides the heat for steam generation. However, in this
155 mode, the solar temperatures are not sufficient to provide superheating; thus, the plant utilizes a
156 secondary firebox to boost the steam temperature for more efficient power production. The system also
157 provides flexible preheating of the boiler feedwater, which is achieved by a combination of recovered
158 heat from solar, steam extraction from the turbines, and waste heat from the boiler via an economizer.
159 While this work does not focus on ISCC, it could be integrated with such a concept by replacing some of
160 the air intake and fuel firing with effluent streams from a gas turbine. However, this is outside of the
161 scope of this work, which seeks to focus on synergistic designs and control of hybrid steam power plants.

162 This work pays special attention to the combination of design and control to ensure that the plant
163 can be economically and reliably operated. Because solar is very transient, control of the plant is non-
164 trivial. Switching from natural gas mode to solar hybrid mode requires extreme changes in operation. The
165 system is designed to seamlessly handle these transitions; i.e., it is coupled with a robust control system
166 that effectively switches between two different energy sources. Often in literature, the control system for
167 solar plants is not developed in detail as the focus is typically on design or performance. A dynamic
168 approach for modeling of solar plants is essential because they are inherently dynamic in nature, given the
169 rapid fluctuations of available sunlight. Because these fluctuations pose great risks to the system
170 reliability, a robust control scheme is necessary to effectively respond to disturbances and continuously
171 produce power efficiently. This study is among the first to investigate hybrid solar/natural gas plant in
172 combination with a closed-loop control scheme.

173 A final objective of this work is to use the system model to quantify the benefits of this hybrid
174 design over an entire year and summarize the key performance indicators, such as solar share and STE.
175 Solar share is also defined as the fraction of the total power production from solar energy. Simulation
176 results demonstrate that the hybrid plant has an improvement of 71.9% in STE over a stand-alone solar
177 plant on an annual basis. This increased STE is because of the higher thermal efficiency observed in the
178 hybrid plant, largely due to gas-fired steam superheating and the various forms of waste heat recovery in
179 the plant. The overall efficiency of the hybrid plant is only 5.9% lower than a pure natural gas plant,
180 indicating a minimum efficiency loss due to hybridization.

181 The remainder of the paper is divided into five sections. Section 2 provides an overview of the
182 system, followed by a description of the model, presented in Section 3. In Section 4, an overview of the
183 control schemes proposed for the different components of the stand-alone and hybrid plants is provided.

184 Then, the simulation results and control performance of the system are illustrated in Section 5. Finally,
185 Section 6 provides a summary of the results and directions for future work.

186 **2. System Overview**

187 The solar thermal and natural gas hybrid power plant, shown in detail in Figure 1, uses a solar
188 field to heat up a thermal oil, or heat transfer fluid (HTF), which is used to transfer heat to a Rankine
189 power cycle. The nominal power production from the Rankine cycle during the night is 100 MW while
190 the plant can produce as much as 140 MW during the day, depending on the received DNI. The solar heat
191 is coupled with natural gas, which provides dispatchability and reliability by being available on demand.
192 In addition to enhanced reliability, natural gas can also improve the solar-to-electric efficiency of the
193 plant, by being used in a synergistic manner. The design presented in this paper uses a dual-fired boiler,
194 with solar heat and natural gas being used by the steam generator to produce steam at 625 K (170 bar)
195 while natural gas is also used in a secondary firebox to superheat and reheat the steam to higher
196 temperatures (824 K) [22]. The superheated steam is then depressurized in three turbines to produce
197 power. This design allows the solar heat to be effectively used within the limits of the heat transfer fluid,
198 resulting in a reduction of the radiative heat losses of the solar field and preservation of the HTF.
199 Additionally, using superheated steam in the Rankine cycle enhances the overall thermal efficiency of the
200 plant. This synergistic design also provides flexibility for the plant to easily shift between a hybrid mode
201 and a solely natural gas mode at night. This increases the overall capacity factor of the plant, allowing it
202 to produce power around the clock.

2.1 Heat Transfer Fluid Loop

The heat transfer fluid is used to generate steam, which occurs through the pipe coils in the steam drum. The steam drum produces saturated steam at 170 bar and 625 K, corresponding to a design temperature of 665 K for the HTF exiting from the parabolic trough solar field. After the heat from the HTF is used to produce steam in the steam drum, the fluid, now at 630 K is used for auxiliary preheating of the boiler feedwater (BFW). The unit used for this purpose, denoted as the solar BFW preheater in Figure 1, is a shell and tube heat exchanger and is used to extract more heat from the HTF before it returns to the parabolic trough. The HTF entering the parabolic trough is nominally at 587 K, although this temperature varies with time. Temperatures of the HTF, when the DNI reaches 900 W/m², are shown in Table 1.

Table 1: Temperatures in the HTF loop during solar operation.

| Location | Temperature (K) |
|--|-----------------|
| Solar field outlet/steam drum inlet | 665 |
| Steam drum outlet/solar BFW preheater inlet | 630 |
| Solar BFW preheater outlet/solar field inlet | 587 |

2.2 Steam Cycle

Steam can also be generated by combusting natural gas in the firebox. The heat of combustion radiates from the flame and combustion air to the downcomer and riser tubes that are used to circulate a saturated mixture of water and steam in and out of the firebox. The heat from natural gas combustion is used to vaporize the water in these tubes. This supplemental gas firing can be varied by using the natural gas firing rate as a manipulated variable to achieve the desired steam flow rate. Once the saturated steam, generated by a combination of solar thermal and natural gas combustion heat, exits the steam drum, it is superheated using an auxiliary firing of natural gas in a secondary firebox. Because the parabolic trough solar field is not capable of achieving temperatures necessary for steam superheating, this is achieved purely by using natural gas. The availability of natural gas for superheating the steam allows the steam cycle to achieve higher temperatures that results in a higher Rankine cycle efficiency. The superheated steam exits the superheater at 824 K. Steam from the superheater enters the high pressure (HP) turbine and the energy released from its depressurization is used to produce power in a generator. Exiting steam from the HP turbine, now at 35 Bar and 595.6 K, is sent back to the reheater to reach a temperature of 824 K. This is because higher temperatures of the entering steam to the intermediate pressure (IP) turbine result in more power production in the generator. The superheated steam from the reheater is then divided between the IP turbine and the closed heat exchanger, also referred as closed feedwater heater. The closed

243 heat exchanger uses the superheated steam to warm up the incoming water and sends it to the high
 244 temperature open BFW preheater. The high temperature BFW preheater uses this hot water to heat up the
 245 incoming water from the low temperature BFW preheater. After power production in the IP turbine,
 246 steam exits the turbine at 7 Bar and 602.5 K.

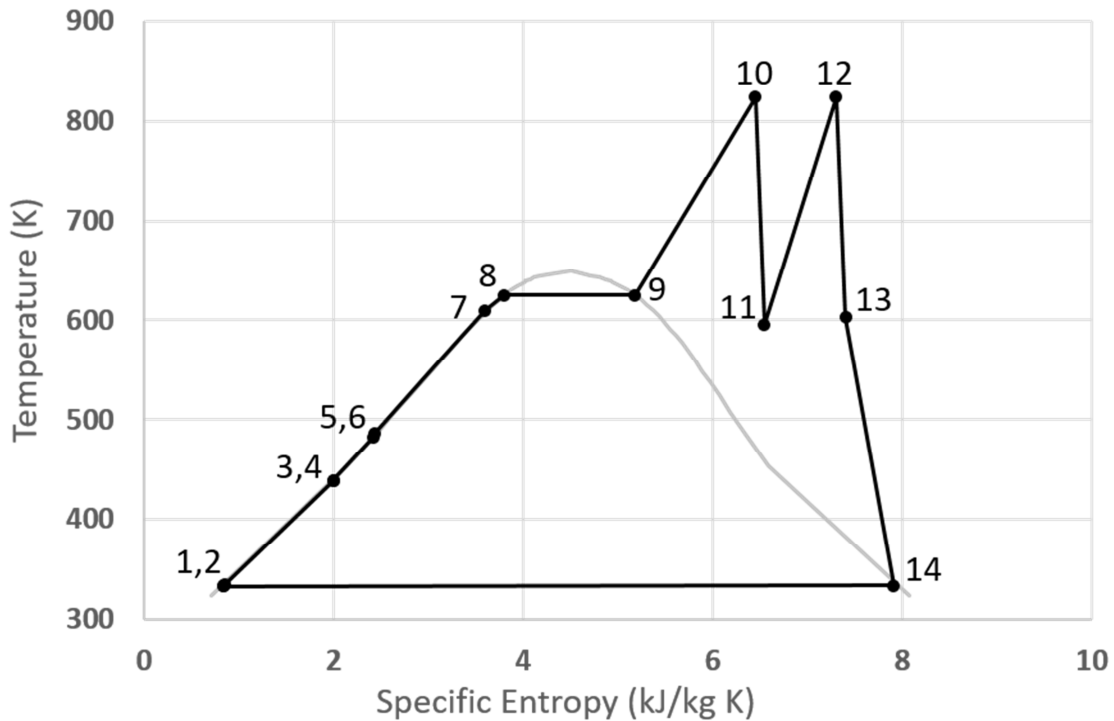
247 Between the IP turbine and the low pressure (LP) turbine, a small fraction of the steam is
 248 extracted and used to preheat the BFW in the low temperature BFW preheater. While this reduces the
 249 power generation from the LP turbine, it is necessary to supplement the heat supply from the economizer
 250 to reach the saturation conditions of the feedwater entering the steam drum. The majority of the steam
 251 exiting from the IP turbine is used to generate power in the LP turbine. The steam that exits the LP
 252 turbine is at 0.2 Bar and 333.3 K before entering the condenser. The condensed water is then pumped
 253 back to 7 Bar. The water is preheated in the solar BFW preheater to make use of the available solar
 254 energy, although a fraction of the steam from the LP turbine is drawn for this purpose when solar energy
 255 is not available. The final stage of boiler feedwater preheating is achieved in an economizer, which
 256 consists of high pressure water tubes passing through the exhaust duct to take advantage of the waste heat
 257 from the combustion process. The economizer outlet temperature is controlled by the amount of natural
 258 gas firing in the secondary firebox with the objective of getting the steam drum inlet temperature to
 259 slightly under the steam saturation temperature. Temperatures, pressures, and the states of the water/steam
 260 streams are summarized in Table 2, while a T-S diagram of the steam cycle is provided in Figure 2. The
 261 control scheme of the entire system is described in detail in Section 4.

262 **Table 2: Temperatures, pressures, and fluid state throughout the steam cycle in hybrid mode. The position**
 263 **numbers correspond to the numbers described in Figure 1.**

| Location | Position | Temp. (K) | Pressure (Bar) | Specific Enthalpy (kJ/kg) | State |
|--|----------|-----------|----------------|---------------------------|----------------------------|
| BFW Pump 1 inlet | 1 | 333 | 0.2 | 250.6 | Slightly sub-cooled liquid |
| Low T BFW preheater input from Pump 1 | 2 | 335 | 7 | 259.5 | Sub-cooled liquid |
| BFW Pump 2 inlet | 3 | 438 | 7 | 696.8 | Sub-cooled liquid |
| High T BFW preheater input from Pump 2 | 4 | 439 | 35 | 702.7 | Sub-cooled liquid |
| BFW Pump 3 inlet | 5 | 482 | 35 | 893.0 | Sub-cooled liquid |
| Solar BFW preheater inlet | 6 | 486 | 170 | 916.0 | Sub-cooled liquid |
| Economizer inlet | 7 | 610 | 170 | 1559.0 | Sub-cooled liquid |
| Steam drum inlet | 8 | 625 | 170 | 1690.0 | Saturated liquid |
| Superheater inlet | 9 | 625 | 170 | 2547.1 | Saturated steam |

| | | | | | |
|---|----|-------|-----|--------|----------------------------|
| HP turbine inlet | 10 | 824 | 170 | 3429.6 | Superheated steam |
| Reheater inlet | 11 | 595.6 | 35 | 3035.1 | Superheated steam |
| IP turbine inlet | 12 | 824 | 35 | 3566.4 | Superheated steam |
| LP turbine inlet | 13 | 602.5 | 7 | 3120.1 | Superheated steam |
| Condenser inlet | 14 | 333.3 | 0.2 | 2609.0 | Slightly superheated steam |
| Closed heat exchanger input from High T BFW preheater | 15 | 476.7 | 35 | 869.1 | Sub-cooled liquid |
| Closed heat exchanger outlet to High T BFW inlet | 16 | 510.2 | 35 | 1023.3 | Sub-cooled liquid |

264



265

266 **Figure 2: A T-S diagram of the steam cycle of the hybrid plant that shows the different thermodynamic states**
 267 **when solar power generation is active. The location numbers correspond to the numbers described in Figure**
 268 **1 and Table 2.**

269 **2.3 Combustion Air Loop**

270 Before air enters the firebox, it is preheated by the exhaust flue gas using a rotating-plate
 271 regenerative air preheater, which allows it to capture additional exhaust heat. The hot air is mixed with
 272 natural gas, as it combusts in the firebox to provide heat for steam generation. The exhaust flue gas from
 273 the firebox travels to a secondary firebox, where additional heat is added via natural gas combustion to
 274 superheat the steam in the superheater and reheater. The system is designed this way because it allows

275 production of steam at a temperature that is achievable with parabolic trough solar heat (625 K).
 276 However, with natural gas combustion, a steam temperature of 824 K is also achievable, resulting in an
 277 efficient Rankine cycle.

278 After the auxiliary firing in the secondary firebox, the hot flue gas stream is split into separate
 279 ducts for superheating and reheating. A damper is used to control the fractions of flue gas going to each
 280 duct and gives the system another actuator so that the steam temperatures from the superheater and
 281 reheater can each be controlled. This is explained in detail in Section 4. The flue gases from the
 282 superheater and reheater are then recombined such that their heat content can be used in the economizer
 283 to preheat the boiler feedwater. Finally, the lowest temperature exhaust flue gas is used in the rotating-
 284 plate regenerative air preheater to harness more energy by preheating the ambient air before it enters the
 285 primary firebox.

286 **3. Model Development**

287 The model is developed and simulated in Matlab with a Simulink interface using fundamental
 288 energy and material balance equations and thermodynamic relationships. Control schemes that use
 289 proportional, integral, and derivative (PID) controllers are also implemented to regulate the plant during
 290 transient operation. The description of the components of the hybrid model is given in the following
 291 sections.

292 **3.1 Parabolic Trough Solar Field**

293 The solar trough consists of a 257,250 m² area to collect the solar power. This area is the
 294 minimum solar collector area required to produce the desirable output temperature of the HTF (665 K).
 295 Therminol VP1 is the heat transfer fluid used in this study. Before sending the heat transfer fluid to the
 296 steam drum, the goal is to achieve a temperature of 665 K for the heat transfer fluid, noting that the
 297 maximum temperature limit of the HTF is 673 K before degradation occurs. An energy balance on the
 298 heat transfer fluid yields the following equation:

$$A_{xs}\rho_{htf}C_{htf}\frac{\partial T_{htf}}{\partial t} = \dot{m}_{htf}C_{htf}\frac{\partial T_{htf}}{\partial x} - h_{htf}\hat{P}_i(T_{htf} - T_{abs}) \quad (1)$$

$$T_{htf}|_{x=0} = T_{inlet}$$

299 where T_{htf} is the temperature of the heat transfer fluid in the absorber pipe, A_{xs} is the inner cross-sectional
 300 area of the absorber tube, ρ_{htf} is the HTF density, C_{htf} is the HTF heat capacity, \dot{m}_{htf} is the mass flow rate
 301 of HTF, h_{htf} is the convective heat transfer coefficient between the HTF and the inner pipe wall, x is the
 302 axial distance, t represents time, and \hat{P}_i is the perimeter of the pipe. In this equation, subscripts “abs”,

303 “i”, and “htf” refer to the properties of the absorber pipe, inner-pipe properties, and heat transfer fluid,
 304 respectively.

305 An energy balance on the absorber pipe, assuming temperature variations occurring only in the
 306 axial direction, is used to solve for the temperature of the absorber pipe:

$$A_{xs,abs} \rho_{abs} C_{abs} \frac{\partial T_{abs}}{\partial t} = h_{htf} \hat{P}_i (T_{htf} - T_{abs}) - \frac{\hat{P}_o}{R_{abs,g}} (T_{abs}^4 - T_g^4) + q'' \cdot w \cdot \eta_{opt} \quad (2)$$

307 where the subscript “o” means outer, “g” refers to glass, $A_{xs,abs}$ is the inner cross-sectional area of the
 308 absorber tube, \hat{P}_o is the outer perimeter of the pipe, and η_{opt} is the optical efficiency of the receiver that
 309 accounts for reflectivity of the mirrors, transmissivity of the glass envelope, absorptivity of the absorber
 310 pipe, and cosine losses, and q'' is the direct solar flux hitting the parabolic mirror, w is the width of the
 311 mirror, and $R_{abs,g}$ is the thermal resistance between the absorber tube and the glass envelope, expressed in
 312 terms of the emissivities of the outer surface of the absorber pipe (ϵ_{abs}) and the inner surface of the glass
 313 envelope (ϵ_g). The thermal resistance is represented by the following equation:

$$R_{abs,g} = \frac{1}{\epsilon_{abs}} + \frac{(1 - \epsilon_g) r_{abs,o}}{\epsilon_g r_{g,i}} \frac{1}{\sigma} \quad (3)$$

314 where $r_{abs,o}$ is the radius of the outer surface of the absorber pipe, $r_{g,i}$ is the radius of the inner surface of
 315 the glass envelope, and σ is the Stefan-Boltzmann constant [24].

316 Finally, an energy balance on the glass envelope, which also only considers temperature
 317 variations in the axial direction, is given by the following equation:

$$A_{xs,g} \rho_g C_g \frac{\partial T_g}{\partial t} = \frac{\hat{P}_{g,i}}{R_{abs,g}} (T_{abs}^4 - T_g^4) - \hat{P}_{g,o} \sigma \epsilon_g (T_g^4 - T_{air}^4) - h_{air} \hat{P}_{g,o} (T_g - T_{air}) \quad (4)$$

318 where $A_{xs,g}$ is the inner cross-sectional area of the glass tube. In the energy balance Equations 1, 2, and 4,
 319 the temperatures T_{htf} , T_{abs} , and T_g are functions of both time and axial distance (x) along the solar
 320 collector. $\hat{P}_{g,i}$ and $\hat{P}_{g,o}$ are the inner and outer perimeter of the glass tube, respectively. The heat transfer
 321 coefficients for the inner absorber pipe (h_{htf}) and outer glass envelope (h_{air}) are calculated using
 322 empirical relations between Reynolds number and Prandtl number [24].

323 To solve the model, the solar field is divided into smaller control volumes, or nodes, and each of
 324 the partial differential equations (PDEs) is approximated by a set of ordinary differential equations
 325 (ODEs). The number of nodes is selected based on a balance between the model accuracy and complexity
 326 to have a reasonable simulation time. The spatial derivatives in Equation 1 are approximated with a

327 backward finite difference approximation. The model is solved in time using a Runge-Kutta numerical
 328 integration. More details on this methodology are available in [5], [6].

329 **3.2 Dual-Fired Boiler**

330 **3.2.1 Steam Drum**

331 In solar mode, the hot heat transfer fluid from the solar field enters the steam drum and delivers
 332 heat to the boiling water in the steam drum through multiple coils. For an individual coil, the temperature
 333 down the length of a single coil can be determined by solving an energy balance. Assuming the tube walls
 334 to have the same temperature as the fluid inside, the energy balance and boundary condition are as follow:

$$A_{xs}\rho_{htf}C_{htf}\frac{\partial T_{htf}}{\partial t} = -\dot{m}_{htf}C_{htf}\frac{\partial T_{htf}}{\partial x} + h_{htf}\hat{P}(T_{sd} - T_{htf}) \quad (5)$$

$$T_{htf}|_{x=0} = T_{inlet}$$

335 where the subscript “sd” refers to the saturated steam conditions in the steam drum.

336 Using a pseudo-steady-state approximation, an energy balance around the entire heat transfer
 337 fluid tube bundle within the steam drum can be used to solve for the steam flow rate:

$$\dot{m}_{stm,solar} = \frac{\dot{m}_{htf}C_{htf}\Delta T_{htf}n_{coils}}{\Delta \bar{h}_{vap}} \quad (6)$$

338 where $\Delta \bar{h}_{vap}$ is the heat of vaporization (on a mass basis) of the saturated mixture, n_{coils} is the number of
 339 steam drum coils, and the subscript “stm, solar” refers to the mass flow rate of the steam due to the solar
 340 heat input.

341 **3.2.2 Firebox**

342 The firebox is used for natural gas combustion to supplement the solar steam generation. It is
 343 comprised of a large combustion chamber surrounded by downcomer and riser tubes that circulate the
 344 liquid/vapor mixture between the steam drum and the firebox. The firebox is sized such that natural gas
 345 combustion can fully provide the heat necessary for maximum power generation, even when solar energy
 346 is not available. In this mode, the plant essentially operates as a conventional steam power plant. The
 347 firebox is modeled as a single-node control volume with the following energy balance equation:

$$V_{FB}\rho_{comb}C_{comb}\frac{dT_f}{dt} = -\dot{m}_{gases}\int_{T_{in}}^{T_f}C_PdT + (Q_{comb} - Q_{rad} - Q_{conv,fb} - Q_{loss}) \quad (7)$$

348 where subscript “comb” refers to combustion, Q_{comb} refers to the heat of combustion from burning the
 349 gas, ρ_{comb} and C_{comb} refer to the density and heat capacity of the combustion fuel, respectively, Q_{rad} and

350 Q_{conv} are the heat delivered from the firebox into the downcomer and riser tubes by radiation and
 351 convection, respectively, Q_{loss} is the heat lost from the firebox to its surroundings, V_{FB} is the volume of
 352 the firebox \dot{m}_{gases} refers to the mass flowrate of the flue gas in the firebox, and T_f refers to the outlet flue
 353 gas temperature of the firebox. In Equation 7, temperature dependent heat capacities and the integral of
 354 the heat capacities are calculated using relationships from [25]. The individual heat transfer terms are
 355 expressed below:

$$Q_{comb} = \dot{m}_{fuel}LHV \quad (8)$$

$$Q_{rad} = \sigma A_{pipe,rad}(\varepsilon_{g,fb}T_{comb}^4 - \varepsilon_p T_{pipe}^4) \quad (9)$$

$$Q_{conv,fb} = h_{fb}A_{pipe,conv}(T_{comb} - T_{pipe}) \quad (10)$$

$$Q_{loss} = UA_{fb}(T_{comb} - T_{amb}) \quad (11)$$

356 where the subscript “amb” refers to ambient temperature, \dot{m}_{fuel} is natural gas flow rate, LHV is the lower
 357 heating value of natural gas, and $A_{pipe,rad}$ and $A_{pipe,conv}$ are the total pipe area that is exposed to
 358 radiation and convection from the firebox gases, respectively. Additionally, $\varepsilon_{g,fb}$ is the emissivity of the
 359 firebox gases, ε_p is the absorptivity of the pipe, h_{fb} is the convective heat transfer coefficient between the
 360 firebox gases and outer pipe, U is the overall heat transfer coefficient for heat losses from the firebox to
 361 ambient, and A_{fb} is the outer surface area of the firebox.

362 To compute the amount of energy transferred into the actual steam, an energy balance is first
 363 computed on the downcomer and riser walls, denoted with the subscript “pipe”. In the following
 364 equation, m_{pipe} is the pipe mass:

$$m_{pipe}C_{pipe} \frac{dT_{pipe}}{dt} = (Q_{rad} + Q_{conv,fb} - Q_{conv,pipe}) \quad (12)$$

$$Q_{conv,pipe} = n_{pipe}h_{pipe}\hat{P}L(T_{pipe} - T_{stm}) \quad (13)$$

365 Steam generation due to natural gas firing is ultimately delivered to the fluid via convection from
 366 the pipe walls ($Q_{conv,pipe}$); thus, the steam flow rate due to natural gas firing ($\dot{m}_{stm,ng}$) is calculated as:

$$\dot{m}_{stm,ng} = \frac{Q_{conv,pipe}}{\Delta\bar{h}_{vap}} \quad (14)$$

367 The total rate of steam generation is that generated via the HTF coils in the steam drum, which
 368 delivers solar heat, plus that generated in the firebox due to natural gas firing:

$$\dot{m}_{stm} = \dot{m}_{stm,solar} + \dot{m}_{stm,ng} \quad (15)$$

369 While not used explicitly in the model, an overall energy balance on the boiler can be used to
 370 quantify the total amount of heat input into the boiler feedwater to vaporize it:

$$Q_{steam} = Q_{in,solar} + Q_{comb} - Q_{loss} \quad (16)$$

371 where Q_{steam} is the total amount of heat input into the boiler feedwater to make steam and $Q_{in,solar}$ is the
 372 total amount of heat delivered to the boiler from the solar heat transfer fluid.

373 3.2.3 Secondary Firebox

374 The secondary firebox is used as an additional heat injection point to ensure that the steam
 375 emerging from the superheater and reheater reaches 824 K. The secondary firebox is generally used in
 376 solar mode, when the primary firebox is not needed, but the solar heat alone is incapable of superheating
 377 the steam to 824 K. The addition of the secondary firebox ensures a high solar share, while still reaching
 378 the steam temperatures required for a high cycle efficiency. An energy balance on the secondary firebox
 379 is provided in the following equation:

$$V_{SFB} \rho_{comb} C_{comb} \frac{dT_f}{dt} = Q_{comb,SFB} - \dot{m}_{gases} \int_{T_{in}}^{T_f} C_P dT - \dot{m}_{injected} \int_{T_{in}}^{T_f} C_P dT - Q_{Loss} \quad (17)$$

380 where the subscript “SFB” refers to the secondary firebox and Q_{Loss} is the heat lost from the secondary
 381 firebox to its surroundings. The terms ρ_{comb} and C_{comb} are also considered to be temperature dependent.
 382 The heat capacities and the integral of the heat capacities are calculated using relations from [25]. The
 383 secondary firebox intakes both the effluent gases from the main firebox and additional air and fuel for its
 384 supplemental firing. The firebox is treated as its own sub-model and it does not have any heat delivery to
 385 steam pipes. Heat delivery occurs in the subsequent superheater and reheater models.

386 3.2.4 Superheater and Reheater

387 The superheater and reheater are modeled as rectangular ducts with counter-flow heat exchange
 388 to the steam coils inside of these ducts. The hot flue gas emerging from the secondary firebox is split into
 389 two separate chambers: one for the steam superheater and one for the reheater, which are modeled
 390 similarly, albeit sized differently, in order to achieve the steam outlet temperature of 824 K for each:

$$A_{xs,pipe_in} \rho_{steam} C_{steam} \frac{\partial T_{steam}}{\partial t} = \dot{m}_{stm} \frac{\partial \bar{h}_{stm}}{\partial x} + n_{pipes} \hat{P}_i h_{in} (T_{pipe} - T_{stm}) \quad (18)$$

$$T_{stm}|_{x=0} = T_{inlet,stm}$$

$$A_{xs,pipe_wall} \rho_{pipe} C_{pipe} \frac{\partial T_{pipe}}{\partial t} = h_{out} \hat{P}_o (T_{gases} - T_{pipe}) - \hat{P}_i h_{in} (T_{pipe} - T_{stm}) \quad (19)$$

$$+ \sigma n_{pipes} \hat{P}_o (\epsilon_g T_{gases}^4 - \alpha_p T_{pipe}^4)$$

$$A_{xs,duct} \rho_{gases} C_{gases} \frac{\partial T_{gases}}{\partial t} = \dot{m}_{gases} C_{gases} \frac{\partial T_{gases}}{\partial x} - n_{pipes} h_{out} \hat{P}_o (T_{gases} - T_{pipe}) - \sigma n_{pipes} \hat{P}_o (\varepsilon_g T_{gases}^4 - a_p T_{pipe}^4) \quad (20)$$

$$T_{gases}|_{x=L} = T_{inlet,gases}$$

391 where the subscript “*stm*” refers to steam within the node, “*steam*” refers to the outlet steam, n_{pipes} are
 392 the number of pipes, and $A_{xs,pipe_in}$, $A_{xs,pipe_wall}$, and $A_{xs,duct}$ refer to the area of the pipes inner side, wall,
 393 and ducts, respectively. The specific enthalpy for steam, \bar{h}_{stm} , as well as its density, ρ_{steam} , and specific
 394 heat capacity, C_{steam} , are calculated from steam tables at the temperature of the corresponding node at
 395 time t . Subscript “*o*” refers to outlet while “*in*” refers to inlet, respectively. ε_g and a_p refer to the
 396 emissivity of gas and absorptivity of the pipe, respectively.

397 The three coupled partial differential equations listed above represent the energy balances on the
 398 steam inside the pipes, the pipe metal, and the gases in the ducts on the outer side of the pipes. Because
 399 the steam and gases enter from opposite sides of the exchangers, their respective boundary conditions (at
 400 the inlet of each fluid) are enforced at different ends of the exchangers. While these models are essentially
 401 counter flow heat exchangers, they are configured such that the pipe inside the duct winds back and forth
 402 once per node, so that in each node, the outer convective heat transfer coefficient h_{out} is evaluated using a
 403 correlation for cross flow, available from [24]. These equations are solved by converting each PDE to a
 404 series of ordinary differential equations by spatial discretization and finite difference approximations. An
 405 overall energy balance on the secondary firebox, superheater, and reheater yields the following equation,
 406 ignoring the heat losses:

$$Q_{sh} + Q_{rh} = Q_{comb,sfb} + Q_{recovered} \quad (21)$$

407 where Q_{sh} and Q_{rh} are the heat added to the superheated and reheated steam, respectively, $Q_{comb,sfb}$ is
 408 the heat added via natural gas combustion in the secondary firebox, and $Q_{recovered}$ is the waste heat
 409 recovered from combustion in the primary firebox and delivered to the superheat and reheat steam tubes
 410 via convection.

411 3.3 Turbines, Generators, and Pumps

412 The system has high, medium, and low pressure steam turbines, which produce mechanical power
 413 by expanding the steam. Each of the turbine models uses real-time lookup table [26] for superheated
 414 steam to evaluate the specific entropy (s_{in}) and specific enthalpy (\bar{h}_{in}) at the inlet temperature and
 415 pressure. The steam then undergoes a near isentropic expansion with a specific increase in entropy of 0.1

416 kJ/kgK for the high and medium pressure turbines, as observed from the TS diagram of Figure 2. This
 417 corresponds to an isentropic efficiency of 87.1% and 88.3%, respectively, under nominal conditions. The
 418 TS diagram also shows that the low pressure turbine has a greater increase in entropy ($0.55 kJ/kgK$) to
 419 prevent the steam from condensation, resulting in an isentropic efficiency of 73.1% under nominal
 420 conditions. It is also important to note that this study does not consider the change in isentropic efficiency
 421 with time, which occurs due to operation conditions. This is because the change in isentropic efficiency
 422 for the time intervals considered in this study is negligible compared to the overall turbine efficiency,
 423 while this assumption could be easily modified when a longer time horizon (~30 years) is being
 424 considered. The specific enthalpy at the outlet (s_{out}) along with the design outlet pressure are used to find
 425 the outlet temperature and outlet enthalpy (\bar{h}_{out}), again via live-lookup steam tables. Using a generator
 426 efficiency (η_{gen}) of 95%, the power produced from each combination of turbine and generator (P_{gen}) is
 427 given as:

$$P_{gen} = \dot{m}_{stm} \eta_{gen} (\bar{h}_{in} - \bar{h}_{out}) \quad (22)$$

428 The power consumed by the boiler feedwater pumps is given as:

$$P_{pump} = \frac{\dot{m}_{bfw} (P_{out} - P_{in})}{\eta_{pump} \cdot \rho_{bfw}} \quad (23)$$

429 where ρ_{bfw} is the water density, η_{pump} is the pump efficiency (55%), and P_{in} and P_{out} are the inlet and
 430 outlet pressures of the pump, respectively. The outlet temperature of the water from the pump can also be
 431 determined from the following equation, where T_{in} is the temperature of water inlet to the pump:

$$T_{out} = T_{in} + \frac{P_{pump} * (1 - \eta_{pump})}{\dot{m}_{bfw} C_p} \quad (24)$$

432

433 **3.4 Economizer, Solar BFW Preheater, and Open BFW Preheaters**

434 Similar to the reheater and superheater, the economizer and solar BFW preheater are modeled as
 435 counter-flow heat exchangers. Their dynamic models are derived by computing an energy balance on the
 436 inner fluid (fluid 1), the pipe wall that divides the fluids, and the outer fluid (fluid 2). These balances are
 437 shown below, where subscripts 1 and 2 refer to water and flue gas, respectively. Following are the
 438 equations for the economizer with $Q_{rad,e}$ being the heat loss due to radiation from the economizer.
 439 $Q_{rad,e}$ is calculated using a similar relationship as presented by Equation 9 by using T_{pipe} and T_2 .

$$A_{xs,pipe,in} \rho_1 C_1 \frac{\partial T_1}{\partial t} = \dot{m}_1 \frac{\partial \bar{h}_1}{\partial x} + n_{pipes} \hat{P}_i h_{in} (T_{pipe} - T_1) \quad (25)$$

$$T_1|_{x=0} = T_{inlet,1}$$

$$A_{xs,pipe_wall}\rho_{pipe}C_{pipe}\frac{\partial T_{pipe}}{\partial t} = h_{out}\hat{P}_o(T_2 - T_{pipe}) - \hat{P}_i h_{in}(T_{pipe} - T_1) + Q_{rad_e} \quad (26)$$

$$A_{xs,duct}\rho_2C_2\frac{\partial T_2}{\partial t} = \dot{m}_2\frac{\partial \bar{h}_2}{\partial x} - n_{pipes}h_{out}\hat{P}_o(T_2 - T_{pipe}) - Q_{rad_e} \quad (27)$$

$$T_2|_{x=L} = T_{inlet,2}$$

440 The solar preheater uses the heat transfer fluid returning from the steam generator to heat up the
 441 incoming water to the preheater. In the solar BFW preheater, water is directed through a tube that is
 442 surrounded by a casing while the heat transfer fluid flows through the space between the tube and casing.
 443 The equations governing the solar preheater are as follow:

$$A_{in,pipe}\rho_{water}C_{water}\frac{\partial T_{water}}{\partial t} = \dot{m}_{water}\frac{\partial \bar{h}_{water}}{\partial x} + n_{pipes}\hat{P}_i h_{in}(T_{pipe} - T_{water}) \quad (28)$$

$$A_{pipe_CA}\rho_{pipe}C_{pipe}\frac{\partial T_{pipe}}{\partial t} = A_{out,pipe}h_{out}(T_{htf} - T_{pipe}) - A_{in,pipe}h_{in}(T_{pipe} - T_{water}) \quad (29)$$

$$A_{out,pipe}\rho_{htf}C_{htf}\frac{\partial T_{htf}}{\partial t} = \dot{m}_{htf}C_{htf}\frac{\partial T_{htf}}{\partial x} - n_{pipes}h_{htf}\hat{P}_o(T_{htf} - T_{pipe}) \quad (30)$$

444 where A_{pipe_CA} , $A_{out,pipe}$ and $A_{in,pipe}$ are the annular cross sectional area between tube and casing, inner
 445 surface area, and the outer surface area of the internal pipe, respectively. An overall energy balance for
 446 each of these boiler feedwater heat exchangers neglecting losses would yield:

$$Q_{bfw} = Q_{hot} \quad (31)$$

447 where Q_{bfw} is the total amount of heat delivered to the boiler feedwater and Q_{hot} is the total amount of
 448 heat recovered from the corresponding hot stream. The corresponding hot streams are exhaust gas in the
 449 case of the economizer, extraction steam in the case of the low and high temperature BFW heaters, and
 450 solar heat transfer fluid in the case of the solar BFW preheater.

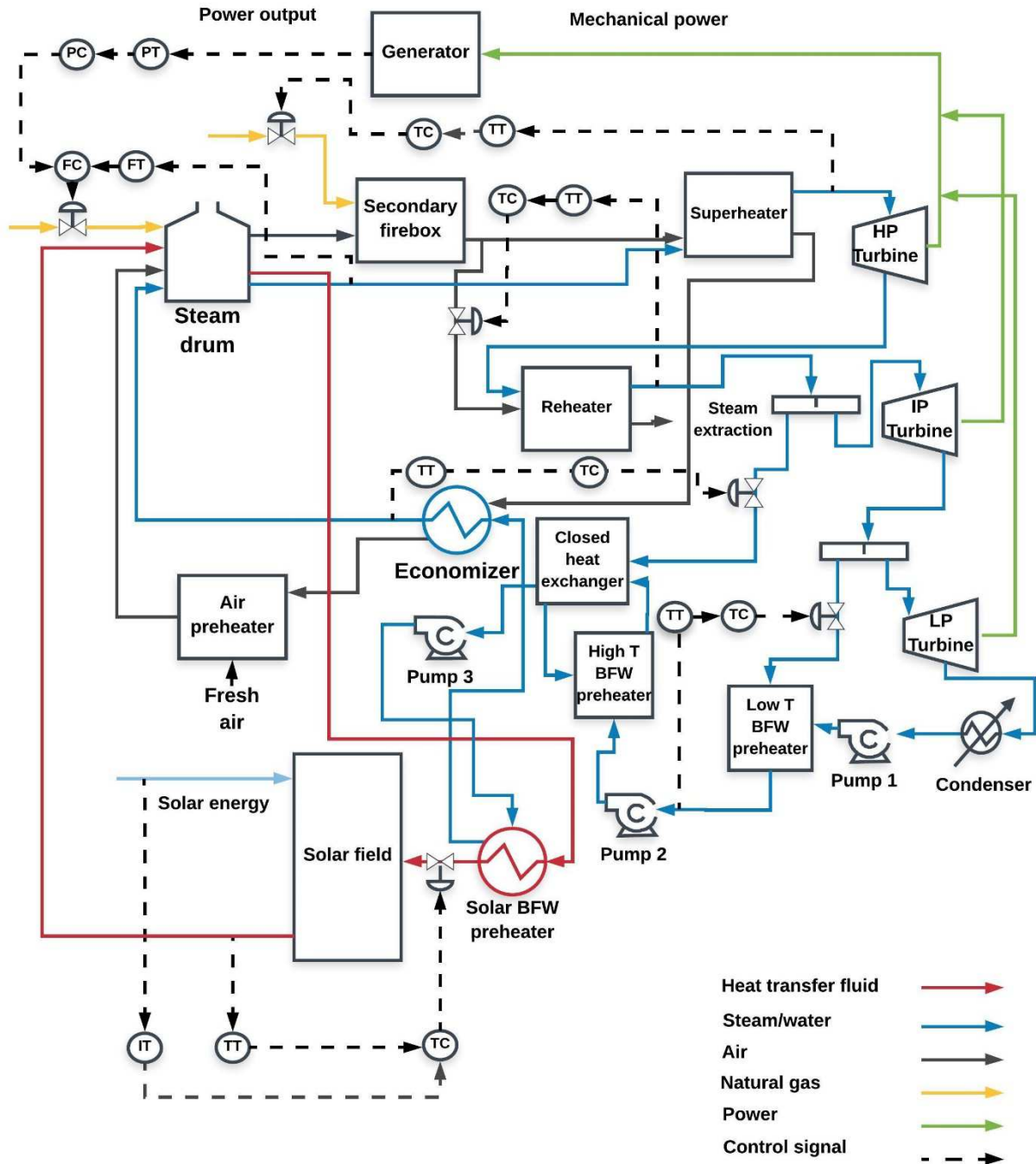
451 The low and high temperature BFW preheaters mix the steam and water and the output is hot
 452 water to be pumped to the next stage. The following equation represents the energy balance of these
 453 preheaters:

$$V_{PH}\rho_{water}C_{water}\frac{\partial T_{water\ out}}{\partial t} = \dot{m}_{water,in}\bar{h}_{water\ in} + \dot{m}_{steam,in}\bar{h}_{steam\ in} - \dot{m}_{water,out}\bar{h}_{water\ out} \quad (32)$$

454 **4. System Controls**

455 Because this work considers the complete dynamics of the plant, it is important to develop a
456 robust control scheme such that the plant can reliably achieve the desired operational state regardless of
457 the external conditions. This is particularly challenging for a solar hybrid plant as it undergoes major
458 changes in operation from a sunny day, when the plant has a high solar energy contribution, to cloud
459 cover or night time, when the plant would rely entirely on natural gas for its energy input. The control
460 scheme of the plant with all of the major control loops is shown in Figure 3 and is described in detail in
461 the following sections.

462



463

464

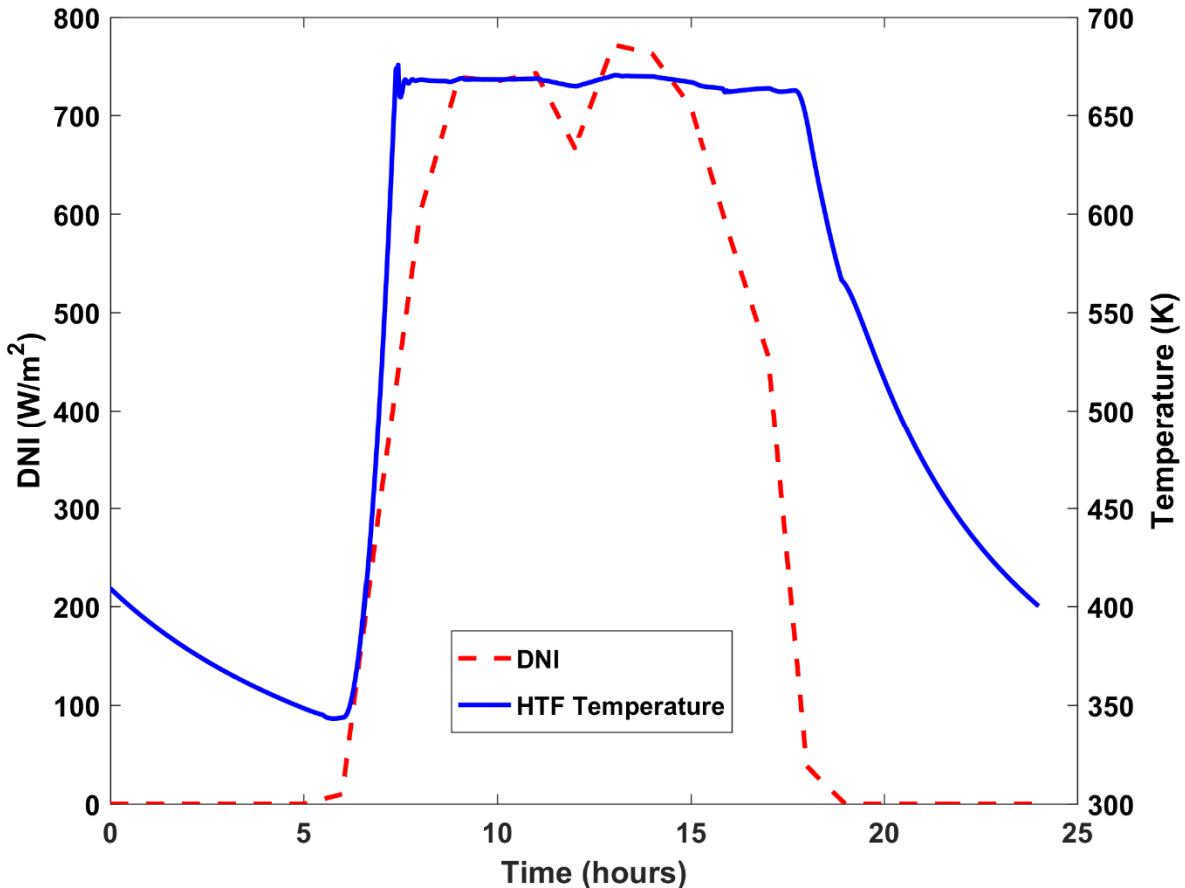
Figure 3: The control scheme of the hybrid plant.

465 4.1 Solar Field Outlet Temperature Control

466 The key disturbance to the plant is the DNI available at the site. This changes drastically over the
 467 course of a day, as observed in Figure 4; thus, it is important to have a control system that can effectively
 468 respond. The first variable impacted by changing the DNI is the solar field outlet temperature. This
 469 temperature is regulated using the total HTF flow rate through the field as a manipulated variable. A

470 feedforward plus feedback control scheme is utilized here. The control scheme uses real time
471 measurements of DNI with an irradiance transmitter (labeled as IT in Figure 3) to proactively respond to
472 changes in DNI. This is coupled with a feedback control loop that uses the measured field outlet
473 temperature, collected by the transmitter TT in Figure 3. The feedback portion of the controller is a
474 proportional-integral (PI) controller that is tuned using internal model control (IMC) tuning
475 recommendations [27]. Temperature is controlled to 665 K as the field temperature when there is enough
476 sunlight. The controller (labeled TC in Figure 3) uses the DNI measurements to proactively adjust HTF
477 flow before a deviation in outlet temperature is observed. The feedback part of the PI controller offsets
478 the effect of additional disturbances such as wind speed and ambient temperature. Figure 4 highlights the
479 temperature control of the solar plant going from sunrise to sunset and demonstrates that this control
480 scheme is quite effective in achieving a constant set point temperature when the Sun is shining. It is also
481 observed that when sunlight is not available, the outlet temperature of the heat transfer fluid reaches to
482 values as low as 350 K.

483



484

485

Figure 4: DNI and solar field outlet temperature over the course of a day (March 27).

486 **4.2 Power Control**

487 Without energy storage, the total solar energy delivered to the system cannot be controlled. To
488 meet the overall power demand, the power from solar energy must be coupled with a supplemental fuel
489 source, which is natural gas in this study. To regulate the total power output from the plant, a cascade
490 control arrangement is used. Power output is measured and sent to a power controller (labeled PC in
491 Figure 3). This PI controller determines the steam flow rate required to achieve its power set point. The
492 signal for the desired steam flow rate is then sent as a set point to a steam flow controller (labeled FC in
493 Figure 3). This steam flow controller is also a PI controller and uses the firing rate of the natural gas in the
494 firebox to achieve the prescribed steam flow rate. Each of these controllers is tuned using the IMC
495 method. This control scheme allows the plant to back off on natural gas firing in the firebox under high
496 DNI conditions. Under these conditions, natural gas flow is nearly zero, although a minimum flow is
497 required to keep the firebox hot. When DNI is low or zero, the firing ramps up to its maximum and the
498 plant transitions from the solar mode to purely natural gas mode.

499 **4.3 Superheater and Reheater Temperature Control**

500 The temperature of steam entering the HP turbine must be carefully regulated to the design
501 conditions, which require an inlet temperature of 824 K. To accomplish this, the superheater steam outlet
502 temperature is linked as a controlled variable (CV) to the natural gas firing rate in the secondary firebox.
503 The firing rate in the secondary firebox also directly influences the reheater steam outlet temperature,
504 which must also be controlled to 824 K. Because the system needs another manipulated variable (MV) to
505 control two CVs, the reheater steam outlet temperature is linked to the damper position in the flue gas
506 ducting. When the reheater steam outlet temperature gets too low, the damper will shift to direct more hot
507 exhaust flue gas to the reheater duct. Each of these control loops is tuned using the IMC method. The
508 temperature of the steam in both reheater and superheater are well maintained at 824 K using the two
509 controllers.

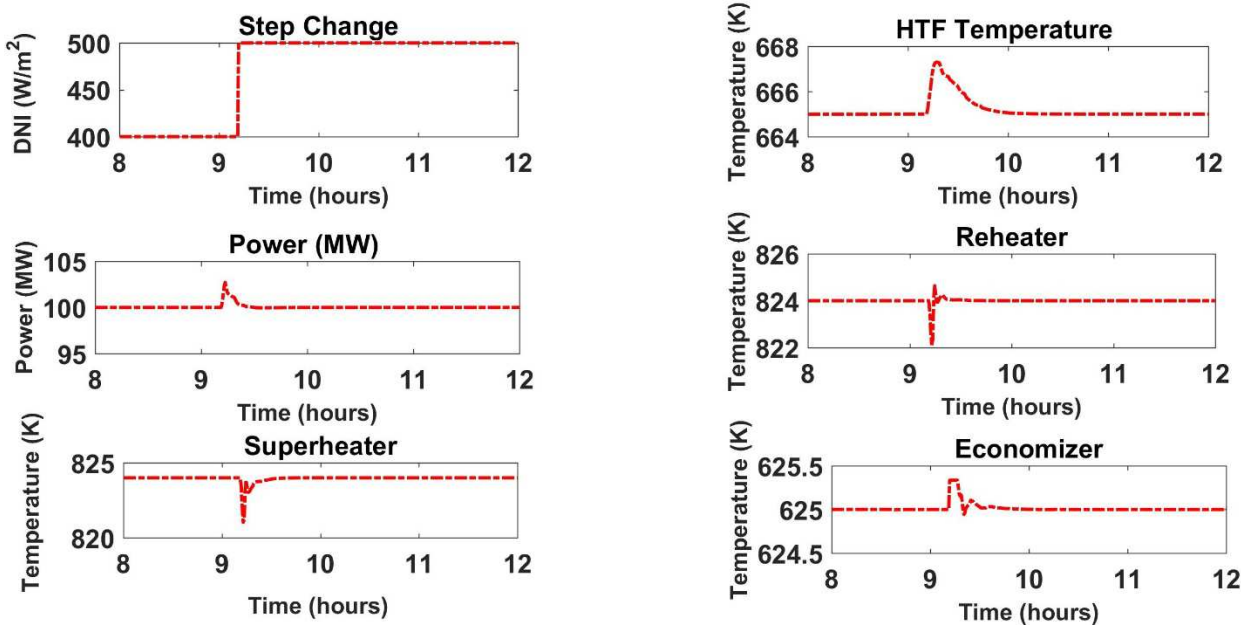
510 **4.4 Steam Drum Inlet Temperature Control**

511 The steam drum consists of a saturated mixture of water and steam. The downcomer and riser
512 tubes are exposed to the heat in the firebox as the mixture circulates and produces a continuous flow of
513 steam. Because the steam drum requires a specific pressure and temperature, it is critical to control the
514 temperature of the incoming boiler feedwater. The temperature of the steam outlet of the steam drum
515 stays around 625 K. Because the boiler feedwater passes through four heat exchanges, including the
516 highly variable solar preheater, control of this temperature is nontrivial. The temperature outlet of the
517 solar preheater fluctuates drastically because it depends entirely on the flow rate of the HTF from the

518 solar trough, which is a function of the available DNI. The economizer outlet temperature can also
 519 fluctuate significantly because it depends on the exit temperature and flow rate of the exhaust flue gas
 520 from the steam drum. The steam flow rate, therefore, is needed as an MV to regulate the low temperature
 521 BFW temperature. This comes at the cost of power production from the LP turbine, but it is necessary to
 522 ensure that the feedwater enters the steam drum at the proper temperature. Because the temperature after
 523 the economizer is the most critical, this is selected as the CV. This temperature is controlled to just below
 524 the steam drum temperature to keep it from vaporizing in the tubes. A single-input single-output (SISO)
 525 feedback controller that links the outlet temperature of the economizer to the fraction of the steam
 526 directed from the IP turbine inlet, adequately controls this temperature. This controller is also tuned with
 527 the IMC tuning relations.

528 4.5 Controller Performance

529 Operation of the plant is complex and the controllers have many interactions. With the DNI
 530 values changing drastically over the course of a day, the entire operation must adapt to regulate the
 531 system as these disturbances occur. As a demonstration of the robustness of the control system outlined
 532 here, transient responses of the major CVs to a sudden and drastic change to DNI are shown in Figure 5.



533
 534 **Figure 5: Step change responses for the major CVs in the plant simulation.**

535 As a step change from 400 to 500 W/m² is introduced to the DNI profile, all of the controllers
 536 must act to overcome the disturbance and return their respective CVs back to their respective set points.
 537 As Figure 5 demonstrates, while all CVs are impacted by this sudden change, none of them experiences

538 major set point deviations; i.e., they all return to their steady-state values within a few minutes. However,
539 it is notable that the temperature of the HTF takes longer to reach to the desired set point in comparison to
540 other CVs.

541 While the distributed SISO controllers obviously experience a lot of interaction, this scheme
542 demonstrates that it is adequate for regulation in these circumstances. However, such interactions suggest
543 that control performance could be improved by considering a multivariable control approach, such as
544 model predictive control. It should be noted, however, that this paper is focused on the dynamic
545 simulation and demonstration of the benefits of plant hybridization and advanced control of the hybrid
546 plant may be considered in future works.

547 **4.6 Stand-Alone Solar Plant**

548 **4.6.1 System Overview**

549 For comparison purposes, a stand-alone solar plant is also simulated. While it has no
550 supplemental fuel source, it is equipped with a two-tank direct TES system to ensure dispatchability. This
551 plant uses a parabolic trough solar field with a total area of 257,250 m² for solar collection, which is
552 equivalent to the hybrid plant. Unlike the hybrid plant, operation of the stand-alone plant is not
553 continuous. The parabolic trough solar field begins operating when the Sun comes up and generates
554 enough heat to achieve the desired outlet temperature of 665 K. When this occurs, the HTF flow valve
555 opens to regulate this temperature. In the morning hours, there is not enough DNI to generate power; i.e.,
556 the power block remains inactive while the hot TES tank fills with the hot HTF. Once there is an adequate
557 amount of stored fluid to begin generating power, HTF begins flowing from the hot TES tank, through the
558 superheater, into the steam generator, and through the solar preheater before returning to the cold TES
559 tank. Because this plant does not have supplemental natural gas firing (as in the secondary firebox of the
560 hybrid plant), it is limited to a steam temperature of 653 K and a pressure of 40 Bar. The superheated
561 steam generated in this process passes through each of the turbines, which produce a total of 23 MW.
562 While the storage unit is dynamic in nature and it allows the plant to use energy on an as-needed basis,
563 the power generation is steady in operation based on the demand. The stand-alone solar plant is shown in
564 Figure 6.

581 predictions of the dynamic model developed in Section 3, The dynamic model is then used to evaluate the
582 performance of the hybrid and stand-alone solar plants based on an entire year. Finally, an economic
583 analysis of the three plants considered in this study is provided.

584 **5.1 Transient Results for a Single Day**

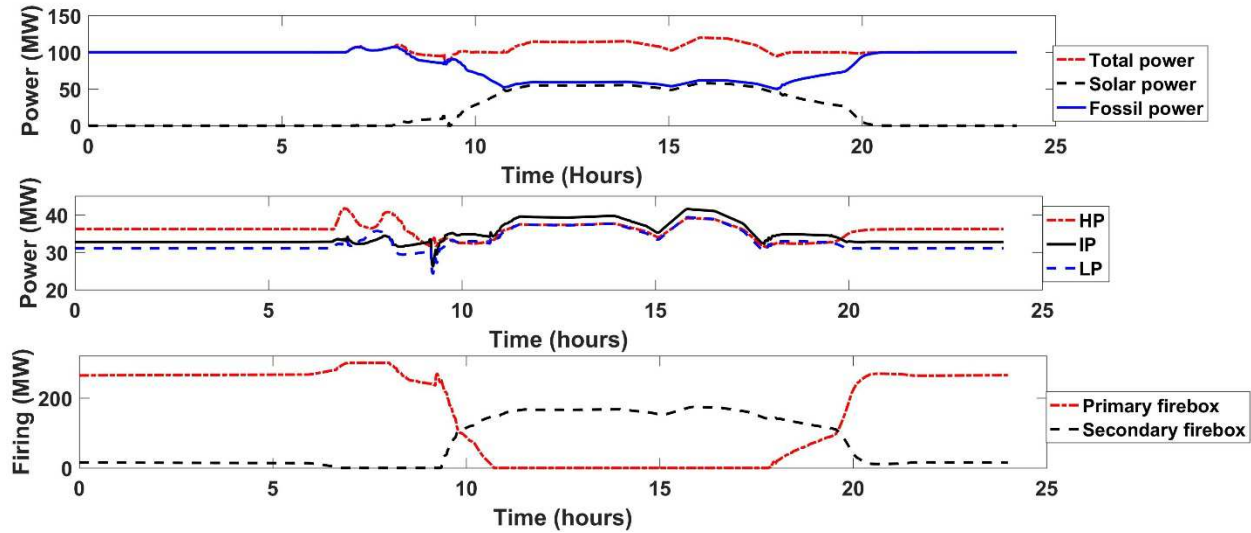
585 First, an analysis of the hybrid plant performance for a single day (March 27) is presented to
586 highlight the short term plant behavior. The power and heat input profiles are shown in Figure 7. As the
587 figure shows, the plant runs entirely on fossil fuel at night, holding at a steady 100 MW. Because the
588 plant is heavily integrated with the solar and gas energy inputs, the power generation from each fuel
589 source must be estimated. This is achieved by using the nominal fuel efficiency (η_{fuel}), which is defined
590 as the gas to electric efficiency when the plant is running in pure natural gas mode. The power production
591 from natural gas (P_{fossil}) is the product of nominal fuel efficiency, natural gas firing rate (\dot{m}_{fuel}), and its
592 lower heating value:

$$P_{fossil} = \eta_{fuel} \dot{m}_{fuel} LHV \quad (33)$$

593 The solar power is the power generated from the solar heat input and is defined as following,
594 where P_{total} is the total power generated from the hybrid plant:

$$P_{solar} = P_{total} - P_{fossil} \quad (34)$$

595 As the Sun comes up, the hot HTF begins flowing through the field and enters the dual-fired
596 boiler and produces steam, which results in some solar power production. The hot HTF flowing through
597 the steam generator immediately causes the total power to rise (due to a higher steam flow rate). The
598 higher power production causes firing in the primary firebox to back off. With less gas being burned in
599 the primary firebox, there is less heat leaving in the exhaust gas. This would cause a decrease in the steam
600 temperature leaving the superheater and reheater, but natural gas firing increases in the secondary firebox
601 to keep these temperatures at their set points of 824 K.

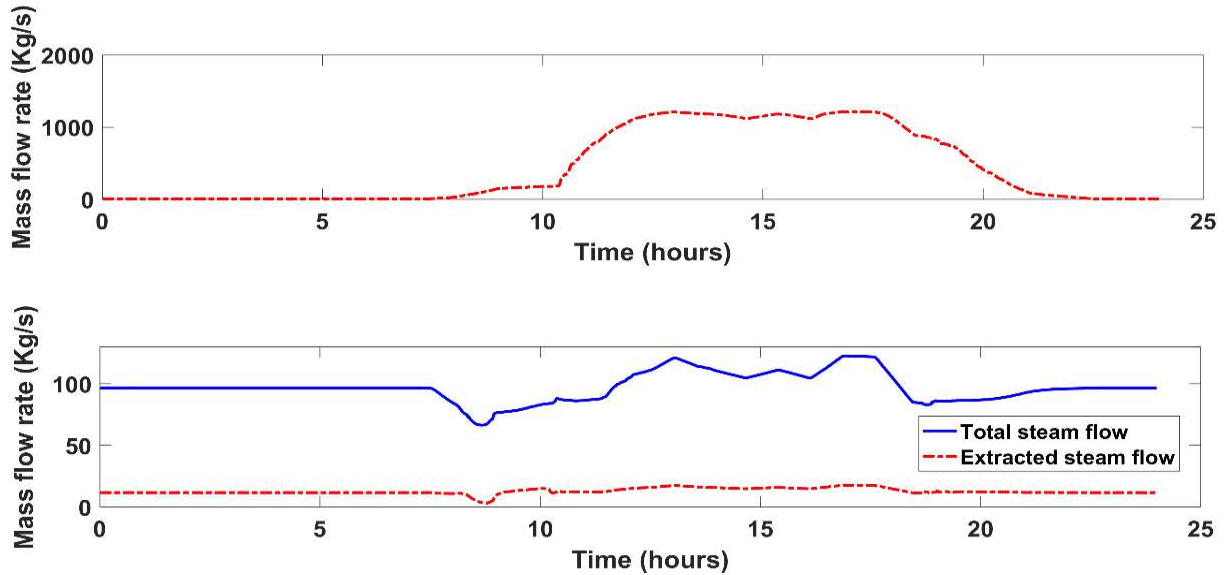


602

603 **Figure 7: Power production and gas firing rates vs. time for the hybrid plant for a day at the end of March.**

604 During peak sunlight hours, the total power exceeds the 100 MW set point. This is because the
 605 flow of HTF through the solar fields gets too high as it is used to regulate temperature. Firing in the
 606 primary firebox ramps down to nearly zero, although a minimal flow is actually used in order to keep the
 607 firebox hot. The main power controller becomes saturated and cannot reduce the main gas flow below this
 608 point, causing it to go above its set point, as Figure 7 shows. The rest of the plant (superheater, reheater,
 609 turbines, etc.) are designed to be able to accommodate this extra heat and continue to produce power. An
 610 alternative operating scenario (and the topic of future work) would be to raise the total power set point
 611 during peak demand hours so that power can be more effectively regulated and the plant can be readily
 612 dispatched to ramp up or down as required by the grid operator.

613 Figure 7 also highlights interesting behavior with respect to the power produced by the various
 614 turbines. At night (in pure gas mode), the high pressure turbine (HP) produces the most power, but this
 615 changes to the intermediate pressure (IP) turbine during solar hours. The cause of this behavior is
 616 attributed to the steam extraction needed for solar BFW preheating. In pure gas mode, extraction of steam
 617 is needed to preheat the BFW; steam is extracted before the IP and LP turbines to feed the high and low
 618 temperature BFW preheaters, respectively. This causes the power output from each of these to decrease
 619 when the plant operates in gas mode. In solar mode, because the HTF exiting the steam drum is
 620 sufficiently hot, it also adds heat to the solar BFW preheater, largely eliminating the need for steam
 621 extraction during sunlight hours. The steam extraction is used in the economizer outlet temperature
 622 control, only when it is needed. As the solar BFW preheater uses solar heat, extraction of steam
 623 automatically backs off, allowing the plant to use energy in the most effective way, while the steam that is
 624 produced previously can be used solely for power production.

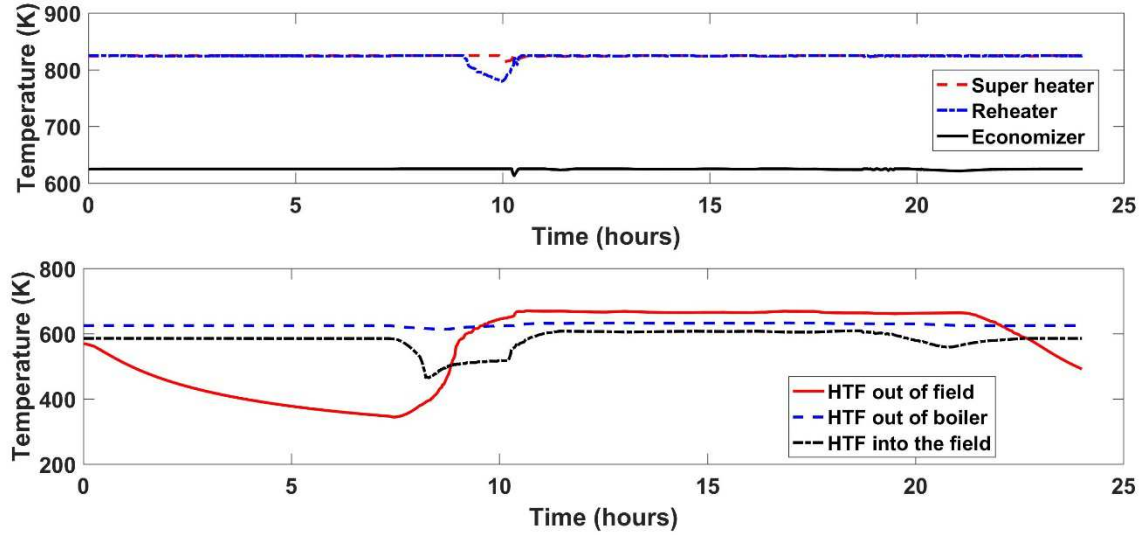


625

626 **Figure 8: HTF flow rate through the solar field (above) and steam flow rate (below) for a day at the end of**
 627 **March.**

628 The top graph in Figure 8 shows that the HTF starts to flow as the DNI increases. This is the
 629 result of the control action of a feedback-feedforward controller that is used to regulate the HTF outlet
 630 temperature. The bottom graph of Figure 8 shows the steam flow rate in the steam generator that is
 631 constant while the plant operates during the night with no disturbance. During day time, the total steam
 632 generation from the solar power and reheater and superheater starts to ramp up with increasing DNI while
 633 an initial dip is also observed, which is because of the control system starting to intervene. Additionally,
 634 the mass extracted steam from the LP turbine inlet slightly increases during day time. This is because the load
 635 on the primary firebox reduces during day time, when the solar power is available. Thus, less hot flue gas
 636 is obtained from the primary firebox leading to a need to extract steam from the LP turbine inlet to
 637 maintain the hot water temperature in the low temperature BFW preheater.

638 Figure 9 indicates an excellent temperature control for the steam/water exiting the superheater,
 639 reheater, and economizer with only minor blips just after the sunrise. The solar field HTF outlet
 640 temperature also exhibits good control during sunlight hours and temperature gradually decreases
 641 overnight as the solar field cools.



642

643 **Figure 9: Temperatures of the HTF, boiler feedwater, and steam at various points in the plant for a day at the**
 644 **end of March.**

645 As expected, the solar share is zero at night, but it increases substantially during daylight hours,
 646 as shown in Figure 10. The solar share peaks and remains at a value close to 48% for a long portion of the
 647 day, which is of substantial importance. The overall efficiency of the plant ($\eta_{overall}$), defined as net
 648 power (P_{net}) produced divided by the sum of the total energy of the gas burned ($\dot{m}_{fuel}LHV$) and the total
 649 solar energy incident ($DNI * A_{field}$) on the field is calculated as following:

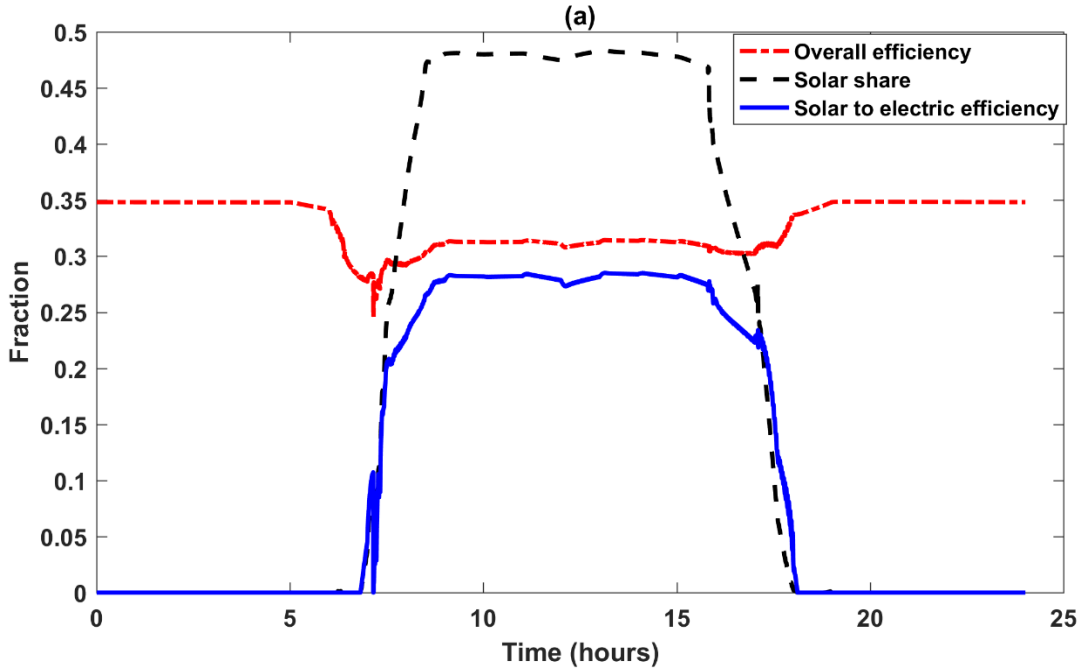
$$\eta_{overall} = \frac{P_{net}}{\dot{m}_{fuel}LHV + DNI * A_{field}} \quad (35)$$

650 It is observed from Figure 10 that the overall plant efficiency is roughly constant at night, as the
 651 plant operates as a gas plant, while it drops during daylight hours. The drop in efficiency is because the
 652 parabolic trough CSP technology has a much lower stand-alone solar-to-electricity efficiency (typically in
 653 the range of 13-18%) [28] as compared to the overall efficiency of the conventional Rankine cycle
 654 technology (typically in the range of 32-36%) [29], [30]. Close inspection of Figure 10 also shows that
 655 the real-time overall efficiency drops before the solar share rises. This is because the initial energy from
 656 the sunlight at dawn is used to raise the temperature of the solar field components; HTF does not actually
 657 flow to generate steam during that period.

658 Although the overall efficiency is reduced in hybrid mode, the real objective of the hybrid plant
 659 design is to improve the efficiency of solar energy delivery. Solar-to-electric efficiency, also referred as
 660 the solar plant stand-alone efficiency (η_{solar}), is a key metric that is used for this purpose. The STE
 661 metric is defined as:

$$\eta_{solar} = \frac{P_{solar}}{DNI * A_{field}} \quad (36)$$

662 It is observed from Figure 10 that the STE reaches a maximum, steady value of 28.4% for the
 663 majority of the day. While it is lower at sunrise and sunset, 28.4% represents a substantial improvement
 664 over existing stand-alone parabolic trough power plants.



665

666 **Figure 10: Solar share, solar-to-electric efficiency and overall efficiency vs. time for a day at the end of**
 667 **March.**

668 5.2 Thermodynamic Analysis of the Plant

669 This section provides a thermodynamic analysis of the system configuration shown in Figure 1 at
 670 steady-state conditions. The purpose of this analysis is to validate the predictions of the model developed
 671 in Section 3 with similar Rankine-based cycles. To achieve this target, a thermodynamic analysis of the
 672 power cycles that is based on enthalpy calculations is utilized, which is consistent with previous studies
 673 [31]. The overall power cycle efficiency is considered as the main validation metric for the purpose of this
 674 analysis. Two cases are considered for this analysis: 1) hybrid solar/natural gas plant, 2) natural gas plant.
 675 The basis for the hybrid mode is a constant DNI of 900 W/m² while a DNI of zero represents the natural
 676 gas plant. To calculate the power cycle efficiency, Equation 35 as well as the energy balance equations of
 677 turbines and pumps (Equations 22 and 23) are still applicable for this analysis. Additionally, the steady-
 678 state energy balance of major heat exchangers of Figure 1 completes the thermodynamic analysis of the
 679 power cycle, although they are not explicitly used in the overall efficiency calculation. The steady-state

680 energy balance of all heat exchangers (on steam/water side) is obtained as follows, where Q^g is the heat
 681 gain/loss from steam/water. Heat losses from the heat exchangers are also ignored in the thermodynamic
 682 analysis of this section. For more details on thermodynamic modeling of Rankine cycles, reference should
 683 be made to [31].

$$m_{out}\bar{h}_{out} = m_{in}\bar{h}_{in} + Q^g \quad (37)$$

684 In this thermodynamic analysis, enthalpies of all streams are obtained from steam tables [26]. It is
 685 critical to mention that the enthalpies of all streams for the hybrid plant are obtained at the same
 686 temperatures and pressures reported in Table 2 for consistency with the results obtained in Section 5.1.
 687 Table 3 provides a summary of the energy balance of major equipment of the configuration shown in
 688 Figure 1:

689 **Table 3: Power plant energy balance (steady-state thermodynamic analysis)**

| Equipment | Hybrid Solar/Natural Gas Mode | | Natural Gas Mode | |
|--------------------------------|-------------------------------|-------------------|------------------|-------------------|
| | Enthalpy In (MW) | Enthalpy Out (MW) | Enthalpy In (MW) | Enthalpy Out (MW) |
| BFW Pump 1 | 22.61 | 23.41 | 20.74 | 21.47 |
| BFW Pump 2 | 73.86 | 74.49 | 67.76 | 68.33 |
| BFW Pump 3 | 102.25 | 104.88 | 117.88 | 128.22 |
| Solar BFW preheater (BFW side) | 104.88 | 178.51 | 128.22 | 161.74 |
| Economizer (BFW side) | 178.51 | 193.51 | 161.74 | 202.29 |
| Steam drum (BFW side) | 193.51 | 291.64 | 202.29 | 304.90 |
| Superheater (steam side) | 291.64 | 392.69 | 304.90 | 446.33 |
| Reheater (steam side) | 347.52 | 408.35 | 378.10 | 426.90 |
| HP turbine | 392.69 | 347.52 | 446.33 | 378.10 |
| IP turbine | 378.04 | 330.73 | 346.80 | 303.40 |
| LP turbine | 281.50 | 235.38 | 258.19 | 216.62 |
| Condenser (steam side) | 235.38 | 22.61 | 216.62 | 20.74 |
| Primary firebox | 0 | - | 353.0 | - |
| Secondary firebox | 188.20 | - | 0 | - |
| Parabolic trough | 231.53 | - | 0 | - |

690 Using the enthalpy information of pumps and turbines from Table 3 as well as the associated
 691 efficiency of each equipment, the overall steady-state efficiencies of the hybrid and natural gas plants are
 692 29.61% and 35.23%, respectively. Both values are well within the range of similar cycles with a simple

693 Rankine cycle [30], [32], [33]. The overall efficiency of the hybrid plant obtained from the dynamic
 694 model of Section 3 (as shown in Figure 10) is also consistent with the thermodynamic efficiency of the
 695 cycle throughout the day; i.e., when in natural gas mode (night time), the efficiency obtained from the
 696 dynamic model is approximately 34.79% while it is in the range of 24.6% to 34.78% in hybrid mode (day
 697 time). This demonstrates that the dynamic model accurately predicts the overall efficiency of the plant
 698 within the range of thermodynamic efficiency of simple Rankine cycles. With the dynamic model
 699 validated thermodynamically, it is next used to investigate the plant behavior for an entire year.

700 **5.3 Annual Performance Results**

701 The closed-loop hybrid plant and the stand-alone plant with storage are simulated for an entire
 702 year with a maximum DNI of 994 W/m² and their results are provided in this section. Mathematical
 703 definitions used to compare the results are annual solar share, annual STE, and annual overall efficiency,
 704 and they are defined below:

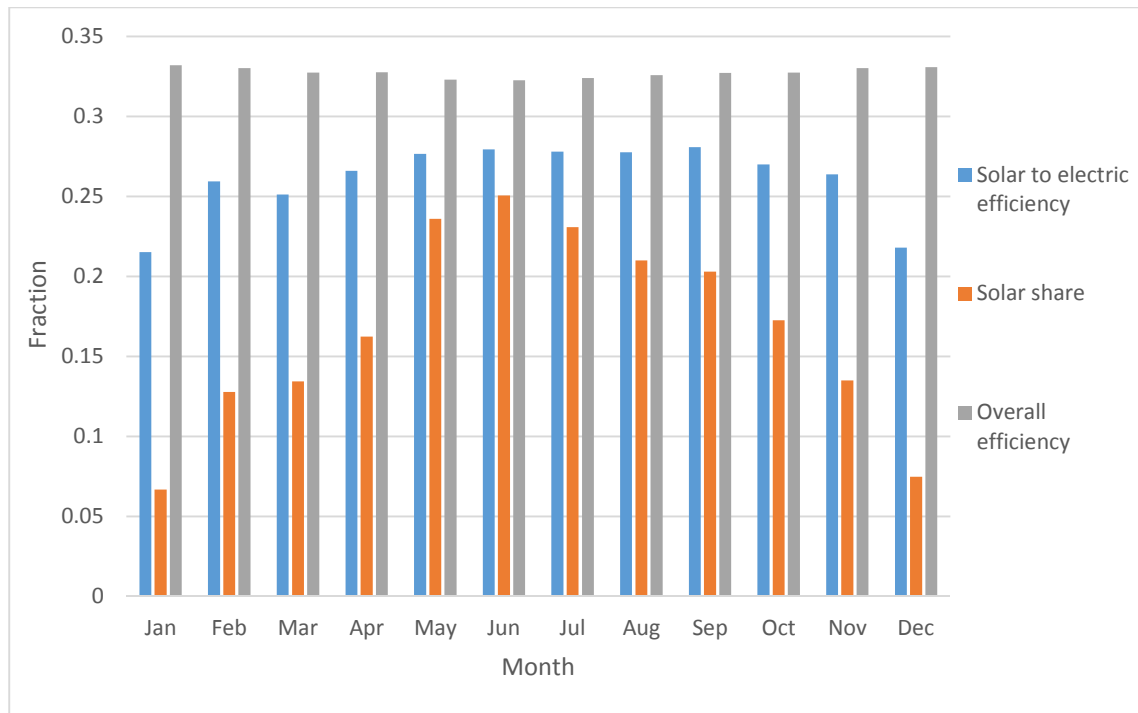
$$Annual\ Solar\ Share = \frac{\int_{t=0}^{t=365\ days} P_{solar} dt}{\int_{t=0}^{t=365\ days} P_{net} dt} \quad (38)$$

$$\eta_{solar,annual} = \frac{\int_{t=0}^{t=365\ days} P_{solar} dt}{\int_{t=0}^{t=365\ days} (DNI * A_{field}) dt} \quad (39)$$

$$\eta_{overall,annual} = \frac{\int_{t=0}^{t=365\ days} P_{net} dt}{\int_{t=0}^{t=365\ days} (\dot{m}_{fuel} LHV + DNI * A_{field}) dt} \quad (40)$$

705 Figure 11 provides the monthly results for the hybrid plant. As expected, the solar share increases
 706 drastically in summer months (approaching 25%) compared to winter months (6-15%). The annual solar
 707 share for the hybrid plant is 0.167, as indicated in Table 3. While this number appears to be low, it is
 708 important to consider that the plant is operating at a baseload of 100 MW for the entire year, while a
 709 stand-alone solar plant would only be operational for a small fraction of the year.

710 As a result of the increased solar heat injection during the summer months, the overall efficiency
 711 dips slightly in these months (Figure 11). While the annual overall efficiency for the hybrid plant is
 712 slightly less than a fuel-only plant, the difference is small, as Table 3 indicates. The overall efficiency for
 713 the hybrid plant, however, is more than double that of the stand-alone solar plant.



714

715 **Figure 11: Monthly solar-to-electric efficiency, solar share, and overall efficiency for the hybrid plant.**

716 The solar-to-electric efficiency for the hybrid plant is above 25% in most months, with the
 717 exceptions being predominantly winter months. In these months, a higher percentage of solar energy goes
 718 into the initial heating of the HTF in the solar field before the power production from solar becomes
 719 operational. The annual value for the solar-to-electric efficiency for the hybrid plant is 26.13%. This is
 720 substantially higher than the 15.2% observed for the stand-alone solar plant. This is a key result of this
 721 work. By operating the plant in hybrid mode, the amount of energy extracted from the Sun is 71.9%
 722 higher than if the plant was operated solely on solar energy. When integrated on a grid-level, this increase
 723 in the solar energy harvest can significantly increase its contribution and value to the power grid.

724

Table 4: Annual results of solar share, solar-to-electric efficiency, and overall efficiency.

| | Solar Share | Solar-to-Electric Efficiency | Overall Efficiency |
|-------------------|-------------|------------------------------|--------------------|
| Fuel Only | 0 | N/A | 0.3477 |
| Solar Only | 1 | 0.152 | 0.152 |
| Hybrid | 0.167 | 0.2613 | 0.3273 |

725 The key reason for the solar-to-electric efficiency to be higher than in a stand-alone plant is that it
 726 has the ability to deliver heat to the power cycle at a higher temperature. The stand-alone plant is limited
 727 to a lower steam temperature of 653 K and is not able to reach the higher cycle efficiencies, which are
 728 dependent on the temperature at which heat is injected. The hybrid plant collects solar heat at the same

729 HTF temperature (665 K) as the stand-alone plant. However, the hybrid plant utilizes natural gas firing in
 730 the secondary firebox (when in solar mode) to boost the steam temperature from 625 K to 824 K, which is
 731 in line with a conventional plant. The plant is therefore able to simultaneously use solar heat and still
 732 achieve a high cycle efficiency for power production because it benefits from natural gas combustion to
 733 upgrade the solar heat.

734 **5.4 Economic Analysis**

735 Economic analysis is important for understanding the practical implementation of the hybrid plant.
 736 This study considers the capital and operational costs of the different components of the three plants
 737 mentioned previously to calculate the levelized cost of electricity (LCOE). The LCOE is calculated using
 738 the following equation:

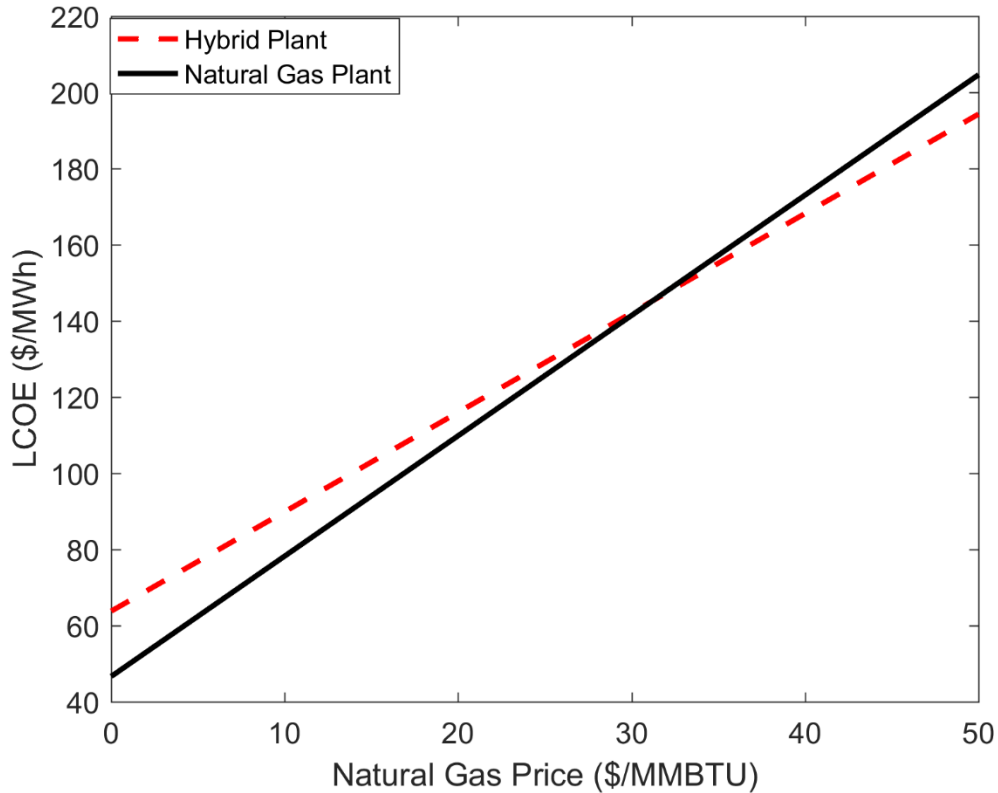
$$LCOE = \frac{\sum_y^m \left\{ \frac{Cost_y^{cap} + Cost_y^{op}}{(1+r)^y} \right\}}{\sum_y^m E_y} \quad (41)$$

739 where m is the lifetime of the plant, $Cost_y^{cap}$ is the capital cost for the year “ y ”, r is the discount rate,
 740 $Cost_y^{op}$ is the operational cost for the year “ y ”, and the total energy generated from the plant in the year
 741 “ y ” is represented by E_y . A summary of the major economic factors, at an assumed natural gas price of
 742 \$2.73/MMBTU, is provided in Table 5.

743 **Table 5: LCOE of different configurations**

| System | Interest for the Yearly Upfront Capital Cost | Upfront Capital Cost (USD/year) | Fuel Cost (USD/year) | Operation and Maintenance Cost (USD/year) | Total Annualized Cost (USD/year) | LCOE (\$/MWh) |
|--------------------------|--|---------------------------------|----------------------|---|----------------------------------|---------------|
| Natural Gas Plant | 7% | \$ 28,353,638 | \$8,504,087 | \$ 9,578,035 | \$46,435,760 | 55.29 |
| Hybrid Plant | 7% | \$ 40,748,804 | \$7,096,392 | \$ 12,338,166 | \$ 60,183,361 | 70.93 |
| Solar | 7% | \$ 11,536,320 | N/A | \$ 8,333,815 | \$ 19,870,134 | \$ 261.17 |

744 As observed from Table 5, the LCOE of the natural gas plant is less than the hybrid plant,
 745 suggesting that the power production from the natural gas plant is still cheaper with the current solar
 746 technologies. A sensitivity analysis on the LCOEs of natural gas and hybrid plants with respect to the
 747 natural gas price is also implemented with the results shown in Figure 12.



748

749 **Figure 12 : The impact of natural gas price on the LCOE of hybrid and natural gas plants for a 100 MW**
 750 **plant**

751 Figure 12 shows that when natural gas price reaches a price of \$31.2/MMBTU, the LCOEs of
 752 both plants break-even at \$145.2/MWh. Considering the current natural gas prices, a value of
 753 \$31.2/MMBTU is far from reality. Hence, this result implies that the natural gas price is not a leveraging
 754 measure for the hybrid plants to compete with natural gas plants. Rather, other financial metrics such as
 755 renewable energy credit and carbon tax might be more effective variables to enable hybrid plants with
 756 justifiable financial metrics against natural gas plants. A detailed economic study on the financial viability
 757 of different plant configurations, while considering the life cycle assessment and the impact of different
 758 green power production policies, is the focus of future work.

759 **6. Conclusions and Future Work**

760 Frequently, renewable energy sources are portrayed as being in contention with fossil fuels.
 761 While it is critical to inject more renewables into the infrastructure of the world over time, a transition
 762 plan may be to consider hybridization at the plant level. This work demonstrates that by designing a plant
 763 that synergistically uses solar energy and natural gas, 71.9% more solar energy is harvested on an annual
 764 basis. This is achieved by comparing a hybrid plant with a stand-alone solar plant under identical

765 environmental conditions and with equivalently-sized parabolic trough solar fields. The design also
766 allows for flexible operation; when natural gas mode is active, the plant essentially operates as a
767 conventional steam cycle power plant, which includes efficiency-enhancing design features. These
768 include heat recovery from the firebox for superheating, steam reheating to extract more power, steam
769 extraction for efficient boiler feedwater preheating, heat recovery by using an economizer, and additional
770 heat recovery by inlet air preheating. When solar mode is active, additional heat at higher temperatures is
771 injected to the cycle through a secondary firebox. This allows the plant to achieve high cycle efficiencies
772 while also utilizing the proven parabolic trough solar technology and injecting high fractions of emission-
773 free energy into the system.

774 Another key benefit of the hybrid plant is reliability. Because it uses a dispatchable fuel (natural
775 gas in this study), which can be fired up as needed, the hybrid plant is able to produce base load power.
776 As the plant makes major transitions from the gas mode (during the night) to solar mode (during the day)
777 on a regular basis, it requires a reliable and robust control system to account for the transient nature of the
778 solar energy. This work develops a dynamic model that captures the dynamic behavior of the solar plant
779 while a control system is also presented for transitioning between the gas and solar modes of operation.
780 Accordingly, the simulation results for a typical day demonstrate that the control system is able to
781 smoothly shift the operation from the gas to solar mode without any major process disruptions.

782 Although the annual solar share (16.7%) of the hybrid plant is modest, it is important to consider
783 that it is based on baseload power, which requires full firing of the natural gas system at night. Noting that
784 the grid power demand is typically lower during the night, the plant may not be needed to operate at full
785 capacity. Thus, power production from the plant can be ramped down at night to a fraction of the 100
786 MW design point, resulting in a higher solar share.

787 With the hybrid design, the contribution of the solar energy in power production can also be
788 increased by increasing the size of the solar field. With time, the plants that are utilizing hybridization
789 concepts can gradually transition to renewable sources. This enables them to become less and less reliant
790 on fossil fuels and move toward emission-free power production. Alternatively, this design can be used
791 directly with biologically-derived gas, making the plant run completely on renewable energy. In addition
792 to increasing the size of the solar field, thermal energy storage can be added. While hybridization
793 provides much of the benefits that thermal energy storage would otherwise provide (e.g. reliability and
794 dispatchability), energy storage would be necessary to achieve near-unity solar shares. The ability to use
795 hybridization and TES synergistically in order to maximize the impact of solar energy will also be
796 considered in future work. It should also be noted that this design relies on natural gas to improve the
797 efficiency of the solar contribution. Higher solar shares in this configuration would result in lesser overall

798 and solar-to-electric efficiency. Other configurations to boost the efficiency would be a solar tower
799 configuration, which can reach higher temperatures with solar and achieve a higher cycle efficiency. This
800 is another topic of future work.

801 Another critical consideration in plant design and operation is the economics of power
802 production. Future work will also include a detailed techno-economic analysis of the hybrid plant in
803 comparison to a fuel-only power plant and a stand-alone solar plant. Economics and efficiency of power
804 production can be improved by utilizing the flexibility of hybridization to optimize operations in real time
805 subject to the environmental conditions.

806 **Acknowledgements**

807 Funding for this project was provided in part by the U.S. Department of Energy's office of
808 Energy Efficiency and Renewable Energy under Grant Number DE-EE0007712 as well as the Utah
809 Governor's Office of Energy Development and the University of Utah. The authors are grateful for these
810 funding sources and recognize them as essential for doing this work.

811 **7. References**

- 812 [1] K. M. Powell, K. Rashid, K. Ellingwood, J. Tuttle, and B. D. Iverson, "Hybrid concentrated solar
813 thermal power systems: A review," *Renew. Sustain. Energy Rev.*, vol. 80, pp. 215–237, Dec. 2017.
- 814 [2] M. Romero-Alvarez and E. Zarza, "Concentrating solar thermal power," *Handb. energy Effic.*
815 *Renew. energy*, pp. 1–21, 2007.
- 816 [3] M. S. Jamel, A. Abd Rahman, and A. H. Shamsuddin, "Advances in the integration of solar
817 thermal energy with conventional and non-conventional power plants," *Renew. Sustain. Energy*
818 *Rev.*, vol. 20, pp. 71–81, Apr. 2013.
- 819 [4] R. E. H. Sims, H.-H. Rogner, and K. Gregory, "Carbon emission and mitigation cost comparisons
820 between fossil fuel, nuclear and renewable energy resources for electricity generation," *Energy*
821 *Policy*, vol. 31, no. 13, pp. 1315–1326, Oct. 2003.
- 822 [5] K. M. Powell and T. F. Edgar, "Modeling and control of a solar thermal power plant with thermal
823 energy storage," *Chem. Eng. Sci.*, vol. 71, pp. 138–145, Mar. 2012.
- 824 [6] K. M. Powell and T. F. Edgar, "Control of a large scale solar thermal energy storage system," in
825 *Proceedings of the 2011 American Control Conference*, 2011, pp. 1530–1535.

- 826 [7] Y. Zhao, H. Hong, and H. Jin, "Evaluation criteria for enhanced solar-coal hybrid power plant
827 performance," *Appl. Therm. Eng.*, vol. 73, no. 1, pp. 577–587, 2014.
- 828 [8] R. Saidur, G. BoroumandJazi, S. Mekhlif, and M. Jameel, "Exergy analysis of solar energy
829 applications," *Renew. Sustain. Energy Rev.*, vol. 16, no. 1, pp. 350–356, Jan. 2012.
- 830 [9] C. Koroneos, T. Spachos, and N. Moussiopoulos, "Exergy analysis of renewable energy sources,"
831 *Renew. Energy*, vol. 28, no. 2, pp. 295–310, Feb. 2003.
- 832 [10] J. H. Peterseim, S. White, A. Tadros, and U. Hellwig, "Concentrated solar power hybrid plants,
833 which technologies are best suited for hybridisation?," *Renew. Energy*, vol. 57, pp. 520–532, 2013.
- 834 [11] H. Price *et al.*, "Advances in Parabolic Trough Solar Power Technology," *J. Sol. Energy Eng.*, vol.
835 124, no. 2, p. 109, May 2002.
- 836 [12] D. Mills, "Advances in solar thermal electricity technology," *Sol. Energy*, vol. 76, no. 1–3, pp. 19–
837 31, Jan. 2004.
- 838 [13] V. Siva Reddy, S. C. Kaushik, and S. K. Tyagi, "Exergetic analysis of solar concentrator aided
839 natural gas fired combined cycle power plant," *Renew. Energy*, vol. 39, no. 1, pp. 114–125, Mar.
840 2012.
- 841 [14] M. K. Gupta and S. C. Kaushik, "Exergetic utilization of solar energy for feed water preheating in
842 a conventional thermal power plant," *Int. J. Energy Res.*, vol. 33, no. 6, pp. 593–604, May 2009.
- 843 [15] J. H. Peterseim, A. Tadros, U. Hellwig, and S. White, "Increasing the efficiency of parabolic
844 trough plants using thermal oil through external superheating with biomass," *Energy Convers.
845 Manag.*, vol. 77, pp. 784–793, Jan. 2014.
- 846 [16] K. Rashid, M. N. Sheha, and K. M. Powell, "Real-time optimization of a solar-natural gas hybrid
847 power plant to enhance solar power utilization," in *2018 Annual American Control Conference
848 (ACC)*, 2018, pp. 3002–3007.
- 849 [17] K. M. Powell, J. D. Hedengren, and T. F. Edgar, "Dynamic optimization of a hybrid solar thermal
850 and fossil fuel system," *Sol. Energy*, vol. 108, pp. 210–218, Oct. 2014.
- 851 [18] K. M. Powell, J. D. Hedengren, and T. F. Edgar, "Dynamic optimization of a solar thermal energy
852 storage system over a 24 hour period using weather forecasts," in *2013 American Control
853 Conference*, 2013, pp. 2946–2951.
- 854 [19] Q. Yan, E. Hu, and R. Zhai, "Evaluation of solar aided thermal power generation with various

- 855 power plants,” *Int. J. Energy Res.*, vol. 35, pp. 909–922, 2011.
- 856 [20] D. Popov, “Innovative solar augmentation of gas turbine combined cycle plants,” *Appl. Therm.*
857 *Eng.*, vol. 64, no. 1, pp. 40–50, 2014.
- 858 [21] G. Zhu, T. Neises, C. Turchi, and R. Bedilion, “Thermodynamic evaluation of solar integration
859 into a natural gas combined cycle power plant,” *Renew. Energy*, vol. 74, pp. 815–824, 2015.
- 860 [22] E. Liese and S. E. Zitney, “Using Dynamic Simulation to Evaluate Attemperator Operation in a
861 Natural Gas Combined Cycle With Duct Burners in the Heat Recovery Steam Generator,” *J. Eng.*
862 *Gas Turbines Power*, vol. 140, no. 1, p. 011801, Sep. 2017.
- 863 [23] “National Solar Radiation Data Base.” [Online]. Available:
864 http://rredc.nrel.gov/solar/old_data/nsrdb/1991-2005/tmy3/. [Accessed: 12-Jun-2018].
- 865 [24] T. L. Bergman and F. P. Incropera, *Fundamentals of heat and mass transfer*. Wiley, 2011.
- 866 [25] D. Himmelblau and J. Riggs, *Basic principles and calculations in chemical engineering*. FT Press,
867 2012.
- 868 [26] “Steam tables,” 2018. [Online]. Available: [http://www.spiraxsarco.com/Resources/Pages/steam-](http://www.spiraxsarco.com/Resources/Pages/steam-tables.aspx)
869 [tables.aspx](http://www.spiraxsarco.com/Resources/Pages/steam-tables.aspx). [Accessed: 13-Jun-2018].
- 870 [27] D. E. Seborg, *Process dynamics and control*. John Wiley & Sons, 2011.
- 871 [28] D. Vallentin and P. Viebahn, “Economic Opportunities Resulting From a Global Deployment of
872 Concentrated Solar Power (CSP) Technologies – The Example of German Technology Providers
873 Economic Opportunities Resulting From a Global Deployment of Concentrated Solar Power
874 (CSP) Technologies ,” *Energy Policy*, vol. 38, no. 8, pp. 4467–4478.
- 875 [29] T. Wang and G. Stiegel, *Integrated gasification combined cycle (IGCC) technologies*. Woodhead
876 Publishing, 2016.
- 877 [30] M. M. K. Fraña, “A Design of the Organic Rankine Cycle for the Low Temperature Waste Heat,”
878 *Int. J. Mech. Aerospace, Ind. Mechatron. Manuf. Eng.*, vol. 8, no. 3, pp. 503–508, 2014.
- 879 [31] P. N. Nwosu, ; A Nurick, and E. T. Akinlabi, “Thermodynamic Optimization Tools for Power
880 Tracking in a Multistage Concentrated Solar Power Rankine Plant,” *J. Energy Eng.*, vol. 143, no.
881 1, p. 04016031, 2016.
- 882 [32] S. M. Safdarnejad, J. D. Hedengren, and K. M. Powell, “Performance comparison of low
883 temperature and chemical absorption carbon capture processes in response to dynamic electricity

884 demand and price profiles,” *Appl. Energy*, vol. 228, pp. 577–592, Oct. 2018.

885 [33] S. M. Safdarnejad, J. D. Hedengren, and L. L. Baxter, “Plant-level dynamic optimization of
886 Cryogenic Carbon Capture with conventional and renewable power sources,” *Appl. Energy*, vol.
887 149, pp. 354–366, Jul. 2015.

888